

# DIFFERENTIAL SIMILARITY IN HIGHER DIMENSIONAL SPACES: THEORY AND APPLICATIONS

L. THORNE MCCARTY  
DEPARTMENT OF COMPUTER SCIENCE  
RUTGERS UNIVERSITY

**ABSTRACT:** This paper presents an extension and an elaboration of the *theory of differential similarity*, which was originally proposed in [McC14, McC18]. The goal is to develop an algorithm for *clustering* and *coding* that combines a geometric model with a probabilistic model in a principled way. For simplicity, the geometric model in the earlier paper was restricted to the three-dimensional case. The present paper removes this restriction, and considers the full  $n$ -dimensional case. Although the mathematical model is the same, the strategies for computing solutions in the  $n$ -dimensional case are different, and one of the main purposes of this paper is to develop and analyze these strategies. Another main purpose is to devise techniques for estimating the parameters of the model from sample data, again in  $n$  dimensions. We evaluate the solution strategies and the estimation techniques by applying them to two familiar real-world examples: the classical MNIST dataset and the CIFAR-10 dataset.

## 1. INTRODUCTION.

This paper presents an extension and an elaboration of the *theory of differential similarity*, which was originally proposed in [McC14, McC18]. The goal is to develop an algorithm for *clustering* and *coding* that combines a geometric model with a probabilistic model in a principled way. The geometric model is a Riemannian manifold with a Riemannian metric,  $g_{ij}(\mathbf{x})$ , which is interpreted as a measure of *dissimilarity*. The probabilistic model consists of a stochastic process with an invariant probability measure that matches the density of the sample

input data. The link between the two models is a potential function,  $U(\mathbf{x})$ , and its gradient,  $\nabla U(\mathbf{x})$ . Since the components of the gradient appear in the definition of the dissimilarity metric, the measure of dissimilarity will depend on the probability measure. Roughly speaking, the dissimilarity will be small in a region in which the probability density is high, and vice versa. Finally, the dissimilarity metric is used to define a coordinate system on the embedded Riemannian manifold, which leads to an “optimal” lower dimensional encoding of the original data.

For simplicity, the geometric model in [McC14, McC18] was restricted to the three-dimensional case, and this was the main deficiency of the theory. The present paper removes this restriction, and considers the full  $n$ -dimensional case. Although the mathematical model is the same, the strategies for computing solutions in the  $n$ -dimensional case are different, and one of the main purposes of this paper is to develop and analyze these strategies. Another main purpose is to devise techniques for estimating the parameters of the model from sample data, again in  $n$  dimensions. We evaluate the solution strategies and the estimation techniques by applying them to two familiar real-world examples: the classical MNIST dataset [LBBH98] and the CIFAR-10 dataset [Kri09].

In the broadest terms, this work is an exploration of the *manifold hypothesis* in deep learning [RDV<sup>+</sup>12] [BCV13] [FMN16]. It is a common observation that real-world data in high-dimensional spaces tends to be concentrated on low-dimensional nonlinear subspaces, and this phenomenon seems to contribute to the success of deep neural networks in image recognition, speech recognition, and other similar tasks.

There are now quite a few algorithms for manifold learning: [SSM98] [TB99] [RS00] [TSL00] [BN03] [Bra03] [DG03] [HR03] [ZZ04] [CL06] [WS06] [CSP<sup>+</sup>10] [CZF10] [YZG10]. These algorithms fall into several categories. Some use global methods: [TSL00] [WS06], while others are primarily local. Some use probabilistic models: [TB99] [HR03] [CSP<sup>+</sup>10], while others are primarily geometric. Among the local geometric algorithms, some are based on the Laplacian [BN03] or the Hessian [DG03], and some are based explicitly on a diffusion process [CL06]. For an analysis of this latter category, see [LW10]. Often, a discrete stochastic process is defined initially on a finite graph (e.g., as a random walk) and the limiting case is shown to be a diffusion on a manifold. See, e.g., [BN05] [HAvL07] [THJ10]. In such algorithms, nonlinear dimensionality reduction is usually achieved by a spectral decomposition of the Laplacian on the graph.

In a recent preprint on nonlinear dimensionality reduction [TJ18], Ting and Jordan develop a general theory for the class of *local spectral methods*: “These methods construct a matrix using only information in local neighborhoods and take a spectral decomposition to find a nonlinear embedding.” The class includes: [RS00] [BN03] [DG03] [ZZ04] [CL06]. Ting and Jordan’s general framework specifies a differential operator on a compact manifold, with a variety of boundary conditions, and they analyze how each method converges from a set of conditions on a local neighborhood graph to an eigenproblem for the differential operator. Distinct methods correspond to distinct operators and distinct boundary conditions. The theory also leads to a ranking of the various algorithms, and the authors conclude that Local Tangent Space Alignment (LTSA) by Zhang and Zha [ZZ04] is the best.

However, if we are investigating the manifold hypothesis in the context of *deep learning*, Bengio and his colleagues argue in [BCV13] that we need a method with very different properties. One problem is the neighborhood graph, which has quadratic complexity. More significantly, any manifold learning algorithm based solely on local neighborhoods is not likely to generalize very well, in a deep network, beyond the initial training data. A better algorithm for deep learning would construct a *parametric* coordinate mapping that takes into account remote data, as well as local neighborhood data. Among the existing algorithms, [BCV13] singles out Local Coordinate Coding (LCC) by Yu, Zhang and Gong [YZG10], which has some similarities to *sparse coding* [OF96]. But most of the discussion in [BCV13] focuses on network architectures that can learn embedded manifolds directly from the structure of the data density itself, known as Regularized Auto-Encoders. Two types are considered: Denoising Auto-Encoders (DAEs) [Vin14] and a specialized form of Contractive Auto-Encoders (CAEs) [AB14], both of which can be shown to compute the gradient of the log of the input probability density.

The theory of differential similarity [McC14, McC18] matches the desiderata advocated by [BCV13] more closely than do the algorithms analyzed in [TJ18]. First, it is not based on neighborhood graphs: It is defined from the start on Euclidean  $\mathbf{R}^n$ . Second, the lower dimensional encodings in the theory are constrained globally as well as locally: In the geometric model, the relationship between the local tangent bundle and the global integral manifold is strictly determined by a classical theorem in differential geometry. In the probabilistic model, the relationship between the local diffusion process and the global probability density is strictly determined by a classical theorem on stochastic processes. The diffusion equation in the theory of differential similarity

has a drift term as well as a Laplacian term, which means that the diffusion has an invariant probability measure, or a stationary probability density, unlike the diffusion in [LW10]. And the gradient of the log of the stationary probability density, which is computed by a DAE [Vin14] or a CAE [AB14] in the deep learning framework, is precisely the vector field,  $\nabla U(\mathbf{x})$ , in the theory of differential similarity. We will return to this point in our discussion of “Future Work” in Section 8.

The balance of the paper is organized as follows: Section 2 is a review of “The Probabilistic Model” and Section 3 is a review of “The Geometric Model” from [McC14, McC18]. If the reader is willing to accept on authority (with citations) a few basic results on stochastic processes and differential geometry, this material should be accessible to anyone with a knowledge of linear algebra and advanced calculus. Section 2 is short, and it includes a simple proof of the basic theorem that we will need, without the extended discussion of stochastic processes in [McC14, McC18]. Section 3 is longer, because it is necessary to extend the geometric model to  $n$  dimensions. We use a form of *prototype coding* for the coordinate system, measuring the *distance* from the *origin* (i.e., the “prototype”) in  $n - 1$  specified *directions*. Thus we define a radial coordinate,  $\rho$ , and the directional coordinates  $\theta^1, \theta^2, \dots, \theta^{n-1}$ , collectively denoted by  $\Theta$ . We refer to this as the  $\rho, \Theta$ , coordinate system.

The paper then turns from theory to applications: “How to Estimate  $\nabla U(\mathbf{x})$  from Sample Data” in Section 4 and “Computing the Geodesic Coordinate Curves” in Section 5. To work with sample data, we borrow a technique from the literature on the *mean shift algorithm* [FH75] [Che95] [CM02]. Once we have an estimate of  $\nabla U(\mathbf{x})$ , everything else in the model can be calculated from its components. In particular, since the coordinate curves are defined by geodesics on the embedded Riemannian manifold, they are determined by the Euler-Lagrange equations for the minimization of the energy functional over the Riemannian metric,  $g_{ij}(\mathbf{x})$ . This is a large system of differential and algebraic equations, in a high-dimensional space, but it can be solved numerically in *Mathematica*.

Finally, Sections 6 and 7 demonstrate how the theory works when applied to real-world examples. Section 6, on the MNIST dataset [LBBH98], shows that our calculations lead to intuitively reasonable results, and Section 7, on the CIFAR-10 dataset [Kri09], adds another wrinkle: We show how to use *quotient manifolds* to build invariance into the geometric model, and we show how to use *product manifolds* to combine low-dimensional solutions into a higher dimensional problem

space, so that our dimensionality reduction techniques can be applied recursively.

## 2. THE PROBABILISTIC MODEL.

The probabilistic model is known in the literature as *Brownian motion with a drift term*. More precisely, it is a *diffusion process* generated by the following differential operator:

$$(1) \quad \mathcal{L} = \frac{1}{2}\Delta + \nabla U(\mathbf{x}) \cdot \nabla$$

where  $\Delta$  is the standard Laplacian expressed in Cartesian coordinates and  $U(\mathbf{x})$  is a scalar potential function. Brownian motion, by itself, is generated by the differential operator  $\frac{1}{2}\Delta$ . But Brownian motion “dissipates,” that is, it has no invariant probability measure except zero. When we add a drift term, which is given here by  $\nabla U(\mathbf{x}) \cdot \nabla$ , the invariant probability measure turns out to be finite and proportional to  $e^{2U(\mathbf{x})}$ . This means that  $\nabla U(\mathbf{x})$  is proportional to the *gradient* of the *log* of the stationary probability density.

There are several ways to analyze this diffusion process, and establish this result. One classical approach is to use Kolmogorov’s *backward* and *forward equations*. See [Kol31]. Kolmogorov’s backward equation is:

$$(2) \quad \begin{aligned} \frac{\partial}{\partial t} w(t, \mathbf{x}) &= \frac{1}{2} \sum_{i,j} a^{ij}(\mathbf{x}) \frac{\partial^2}{\partial x^i \partial x^j} w(t, \mathbf{x}) + \sum_i b^i(\mathbf{x}) \frac{\partial}{\partial x^i} w(t, \mathbf{x}) \\ &= \mathcal{L} w(t, \mathbf{x}), \text{ with initial condition } w(0, \mathbf{x}) = f(\mathbf{x}), \end{aligned}$$

in which  $\mathbf{a}(\mathbf{x})$  is a matrix of diffusion coefficients and  $\mathbf{b}(\mathbf{x})$  is a vector of drift coefficients. Notice that the operator  $\mathcal{L}$  in (1) is a special case of the operator  $\mathcal{L}$  in (2). Kolmogorov’s forward equation is:

$$(3) \quad \begin{aligned} \frac{\partial}{\partial t} p(t, \mathbf{x}) &= \frac{1}{2} \sum_{i,j} \frac{\partial^2}{\partial x^i \partial x^j} a^{ij}(\mathbf{x}) p(t, \mathbf{x}) - \sum_i \frac{\partial}{\partial x^i} b^i(\mathbf{x}) p(t, \mathbf{x}) \\ &= \mathcal{L}^* p(t, \mathbf{x}), \end{aligned}$$

in which  $\mathcal{L}^*$  is the formal adjoint of  $\mathcal{L}$ , and  $p(t, \mathbf{x})$  is a probability density equal, in the limit, as  $t \rightarrow 0$ , to the unit probability mass at  $\mathbf{x}$ . To find the stationary probability density of our diffusion process, we need to specialize the operator  $\mathcal{L}^*$  in (3) to the formal adjoint of the operator  $\mathcal{L}$  in (1), and then set  $\partial p / \partial t = \mathcal{L}^* p = 0$ . But if  $\mathbf{a}(\mathbf{x})$  is a constant matrix, then the right-hand side of (3) can be expanded and

simplified to

$$\frac{1}{2} \sum_{i,j} a^{ij}(\mathbf{x}) \frac{\partial^2}{\partial x^i \partial x^j} p(\mathbf{x}) - \sum_i \left( \frac{\partial}{\partial x^i} b^i(\mathbf{x}) \right) p(\mathbf{x}) - \sum_i b^i(\mathbf{x}) \left( \frac{\partial}{\partial x^i} p(\mathbf{x}) \right)$$

If we now set  $\mathbf{a}(\mathbf{x})$  equal to the identity matrix and  $\mathbf{b}(\mathbf{x}) = \nabla U(\mathbf{x})$ , it is a straightforward computation to verify that  $\mathcal{L}^*(e^{2U(\mathbf{x})}) = 0$ .

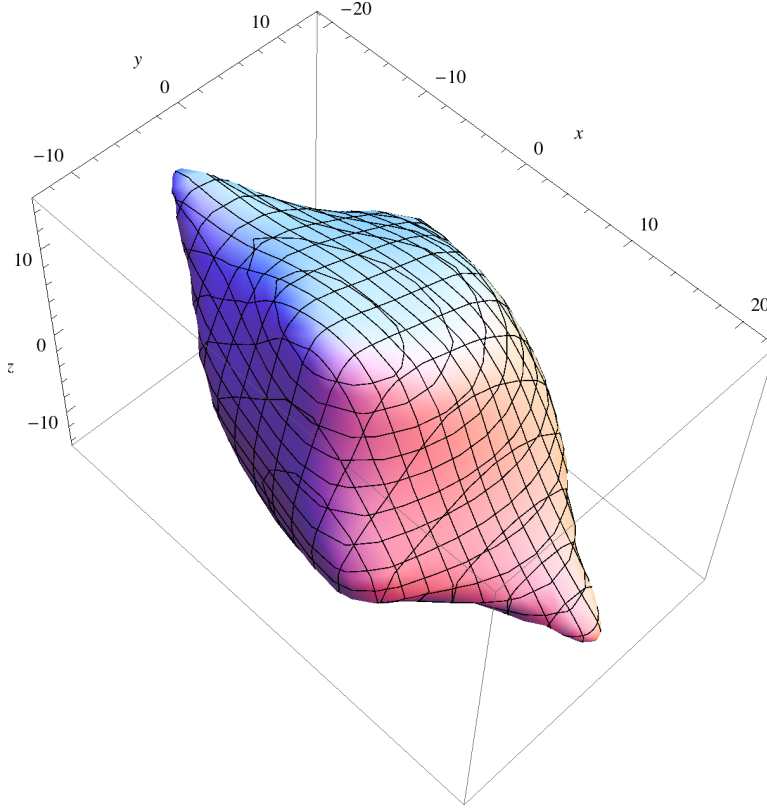


FIGURE 1. Contour plot for the surface of a curvilinear Gaussian potential.

Figure 1 is a three-dimensional example borrowed from [McC18]. The potential function  $U(\mathbf{x})$  is defined here as a quadratic polynomial over the variables  $u$ ,  $v$ , and  $w$ , where

$$u = u(x, y, z), \quad v = v(x, y, z), \quad w = w(x, y, z),$$

is defined as a cubic polynomial coordinate transformation from  $(x, y, z)$  to  $(u, v, w)$ . Thus  $U(\mathbf{x})$  is a sixth-degree polynomial in  $x$ ,  $y$ , and  $z$ , and the gradient,  $\nabla U(\mathbf{x})$ , is a fifth-degree polynomial. We call this the *curvilinear Gaussian potential*. One important property of this potential function is the fact that  $\nabla U(x, y, z) = (0, 0, 0)$  at the origin, which

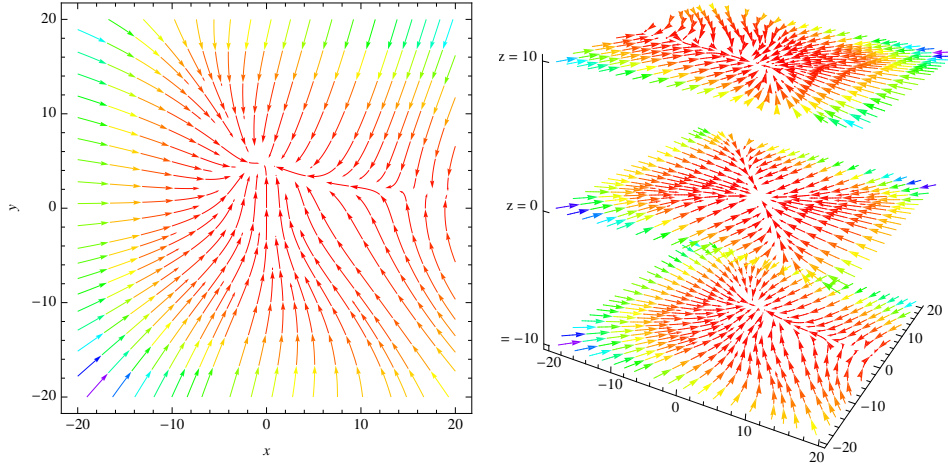


FIGURE 2. Gradient vector field for the curvilinear Gaussian potential: (a) at  $z = -10$ ; (b) at  $z = 10$ ,  $z = 0$  and  $z = -10$ .

means that  $U(0, 0, 0) = 0$  is an extremal point, a maximal point, in fact. Figure 1 is a contour plot for the surface at  $U(x, y, z) = -10$ . Figure 2(a) shows a `StreamPlot` of the gradient vector field generated by  $\nabla U(x, y, z)$  at  $z = -10$ , and Figure 2(b) shows a stack of such stream plots, at the values  $z = 10$ ,  $z = 0$  and  $z = -10$ . Notice how the drift vector twists and turns to counteract the dissipative effects of the diffusion term, and maintain an invariant probability measure.

Looking at Figure 2, an interesting idea comes to mind: Could we use this gradient vector field to define a three-dimensional,  $\rho$ ,  $\Theta$ , coordinate system? The radial coordinate,  $\rho$ , would follow the gradient vector,  $\nabla U$ , and the directional coordinates,  $\theta^1$ ,  $\theta^2$ , would be orthogonal to  $\rho$ . We will see how to do this in Section 3.

The simple formula in (1) is all the reader needs to know about stochastic processes in order to understand the rest of this paper, including the examples in Sections 6 and 7, *infra*. However, Equation (1) is part of a much broader and deeper mathematical subject, discussed in Section 2 of [McC18]. Here is a summary, which could be skipped on a first reading:

**Section 2.1** of [McC18] discusses the connection between Equation (1) and the Feynman-Kac formula [Fey48] [Kac49].

Specializing the operator  $\mathcal{L}$  in (2) to the operator  $\mathcal{L}$  in (1), we have:

$$(4) \quad \frac{\partial w}{\partial t} = \frac{1}{2} \Delta w + \nabla U(\mathbf{x}) \cdot \nabla w, \text{ with } w(0, \cdot) = f.$$

Now consider the following partial differential equation:

$$(5) \quad \frac{\partial u}{\partial t} = \frac{1}{2} \Delta u - V(\mathbf{x}) u, \text{ with } u(0, \cdot) = g,$$

where  $V(\mathbf{x}) = \frac{1}{2} (\Delta U(\mathbf{x}) + |\nabla U(\mathbf{x})|^2)$ . We can show, by a straightforward calculation, using the definition of  $V(\mathbf{x})$  in terms of  $U(\mathbf{x})$ , that  $w(t, \mathbf{x})$  is a solution to (4) if and only if  $e^{U(\mathbf{x})} w(t, \mathbf{x})$  is a solution to (5) with initial value  $u(0, \cdot) = e^U f$ . See Lemma 1 in [McC18]. The Feynman-Kac formula associated with (5) is:

$$(6) \quad u(t, \mathbf{x}) = \int_{\Omega} g(X_t) \exp \left[ - \int_0^t V(X_s) ds \right] \mathcal{W}_{\mathbf{x}}(dX),$$

where  $X_t \equiv X(t, \omega)$  denotes a continuous path in  $\mathbf{R}^n$ , and  $\mathcal{W}_{\mathbf{x}}$  denotes Wiener measure over all such paths beginning at  $X_0 = \mathbf{x}$ . Assuming mild regularity conditions, the theorem of Kac [Kac49], inspired by Feynman [Fey48], states that  $u(t, \mathbf{x})$  as defined by (6) is a solution to (5). Furthermore, because of the relationship between (4) and (5), there is a similar integral, involving both  $U(\mathbf{x})$  and  $V(\mathbf{x})$ , that provides a solution to (4). See Theorem 1 in [McC18].

These equations all have their origins in physics. For example, Equation (5) is a real-valued version of the Schrödinger equation:

$$(7) \quad \frac{\hbar}{i} \frac{\partial \psi(t, \mathbf{x})}{\partial t} = \frac{\hbar^2}{2m} \Delta \psi(t, \mathbf{x}) - V(\mathbf{x}) \psi(t, \mathbf{x}),$$

and Equation (6) with an  $i$  in the exponent is Feynman's famous "path integral" interpretation of quantum mechanics. (A more familiar version of Schrödinger's equation can be obtained by multiplying both sides of Equation (7) by  $i^2 = -1$ .) The Kolmogorov forward equation, Equation (3), is known to physicists as the Fokker-Planck equation. Not as well known, even to physicists, is Chapter 10 of [FH65], in which Feynman and Hibbs analyze a representation of the statistical density matrix in quantum statistical mechanics by means of a real-valued path integral in the form of Equation (6). The existence of these mathematical models in physics leads to a speculative conjecture: Could there be a physical device, at the molecular level, perhaps, that could compute analog solutions for various quantities associated with Equation (1)?

**Section 2.2** of [McC18] discusses the interpretation of Equations (1) and (2) as *stochastic differential equations*, following the theories of both Itô [Ito51] and Stratonovich [Str66].

Itô's theory starts with the definition of a *stochastic integral* in the following form:

$$X(t) = X(0) + \int_0^t \sigma(s, \omega) d\mathcal{B}(s, \omega) + \int_0^t b(s, \omega) ds,$$

where the first integral is an *Itô integral* defined with respect to the Brownian motion  $\mathcal{B}(t, \omega)$ . In differential notation, this would be:

$$dX(t) = \sigma(t, \omega) d\mathcal{B}(t, \omega) + b(t, \omega) dt.$$

Extending the notation to  $n$  dimensions, let  $\mathcal{B}_1(t, \omega), \dots, \mathcal{B}_d(t, \omega)$  be  $d$  independent Brownian motion processes, and define the  $n$ -dimensional *Itô process* as follows:

$$(8) \quad dX(t) = \begin{pmatrix} \sigma_1^1 & \dots & \sigma_d^1 \\ \vdots & & \vdots \\ \sigma_1^n & \dots & \sigma_d^n \end{pmatrix} \begin{pmatrix} d\mathcal{B}_1(t) \\ \vdots \\ d\mathcal{B}_d(t) \end{pmatrix} + \begin{pmatrix} b^1 \\ \vdots \\ b^n \end{pmatrix} dt$$

In this equation,  $\sigma: \mathbf{R}^n \rightarrow \mathbf{R}^{n \times d}$  is the “square root” of  $\mathbf{a}$ , that is,  $\mathbf{a}(\mathbf{x}) = \sigma(\mathbf{x})\sigma(\mathbf{x})^T$ . One basic result of Itô's theory is that Equation (8) defines the same stochastic process as the operator  $\mathcal{L}$  in Equation (2). See Theorem 2 in [McC18].

For our purposes, however, the Itô process has a defect: It is not invariant under coordinate transformations. An alternative is to use the stochastic integral proposed by Stratonovich [Str66]. (Technically, in the discretization of  $t$  that leads to the definition of the integral for  $d\mathcal{B}(s, \omega)$ , Itô's theory evaluates the integrand at the initial point of the interval  $[t_j, t_{j+1}]$ , while Stratonovich's theory evaluates it at the mid point.) A common notation for this alternative is:

$$(9) \quad dX(t) = \begin{pmatrix} \sigma_1^1 & \dots & \sigma_d^1 \\ \vdots & & \vdots \\ \sigma_1^n & \dots & \sigma_d^n \end{pmatrix} \circ \begin{pmatrix} d\mathcal{B}_1(t) \\ \vdots \\ d\mathcal{B}_d(t) \end{pmatrix} + \begin{pmatrix} \tilde{b}^1 \\ \vdots \\ \tilde{b}^n \end{pmatrix} dt$$

It turns out that the Stratonovich integral satisfies a formula for the “chain rule” that is consistent with the Newton-Leibniz calculus, and thus Equation (9) behaves properly under coordinate transformations. Fortunately, we can use both theories, and translate back and forth between the two of them, because (8) and (9) define the same stochastic process whenever

$$\tilde{b}^i = b^i - \frac{1}{2} \sum_{k=1}^d \sum_{j=1}^n \frac{\partial \sigma_k^i}{\partial x^j} \sigma_k^j.$$

See Lemma 2 in [McC18]. This translation can therefore be used to rewrite in a nonlinear  $\rho, \Theta$ , coordinate system any stochastic process that was initially defined by Equation (1) in Euclidean  $\mathbf{R}^n$ .

In particular, Section 6 in [McC18] shows how to convert the example in Figure 1 from an Itô equation in Euclidean  $\mathbf{R}^3$  into a Stratonovich equation in the coordinates  $(\rho, \Theta)$ , and then back into an Itô equation with coefficients  $\alpha^{ij}(\rho, \Theta)$  and  $\beta^i(\rho, \Theta)$ . One interesting consequence of these conversions is the calculation of the “drift correction vector field” illustrated in Figure 18 in Section 6 of [McC18].

**Section 2.3** of [McC18] discusses *integral curves* and *martingales* on manifolds, and develops another interpretation of Equation (1) based on Stroock’s Theorem 7.3.10 in [Str93]. See Theorem 4 in [McC18]. This interpretation is not actually used in [McC18] to justify additional calculations. However, it is likely that Stroock’s work will be useful if we want to advance our theoretical understanding of how the stochastic process generated by Equation (1) interacts with the geometric model that we will construct in Section 3. Our coordinate system for the geometric model is based on integral curves, as we will see, and thus the papers of Stroock and Taniguchi [ST94][ST96] are highly relevant.

### 3. THE GEOMETRIC MODEL.

To implement the idea of prototype coding in our geometric model, we need to define a radial coordinate,  $\rho$ , and the directional coordinates,  $\theta^1, \theta^2, \dots, \theta^{n-1}$ , where  $n$  is the dimensionality of the initial Euclidean space. But what we really want is a lower dimensional subspace, a  $k$ -dimensional subspace, say, where  $k < n$ . Somehow, we would like to choose  $k - 1$  out of the  $n - 1$  directional coordinates, and project our diffusion process onto the resulting  $k - 1$  dimensional space, which can then be combined with our one-dimensional radial coordinate to give us a  $k$ -dimensional subspace. How should these coordinate systems be defined?

First, we want the radial coordinate,  $\rho$ , to follow the drift vector,  $\nabla U(\mathbf{x})$ . To do this, we define  $\rho(t)$  to be the *integral curve* of the vector field  $\nabla U(\mathbf{x})$ , starting at some initial point  $\mathbf{x}_0$ . More specifically, we define  $\rho(t)$  to be the solution to the following differential equation:

$$(10) \quad \begin{aligned} \rho'(t) &= \frac{\nabla U(\rho(t))}{|\nabla U(\rho(t))|} \\ \rho(0) &= \mathbf{x}_0 \end{aligned}$$

or, equivalently, the solution to the following integral equation:

$$(11) \quad \rho(t) = \mathbf{x}_0 + \int_0^t \frac{\nabla U(\rho(s))}{|\nabla U(\rho(s))|} ds, \quad 0 \leq t$$

Since the vector field in (10) or (11) is normalized, the integral curve that solves these equations will be parametrized by Euclidean arc length. However, the parametrization that we choose is just a matter of convenience, and what we really want is a generalization of the concept of an integral curve, known as an *integral manifold*. A one-dimensional integral manifold is, roughly speaking, just the image of an integral curve without the parametrization, and it always exists, for any vector field.

For the directional coordinates,  $\theta^1, \theta^2, \dots, \theta^{n-1}$ , the obvious generalization would be an integral manifold of dimension  $n - 1$ , orthogonal to the integral manifold for  $\rho$ . But, for  $k \geq 2$ , a  $k$ -dimensional integral manifold exists if and only if certain conditions are satisfied, known as the *Frobenius integrability conditions*. Fortunately, as we will see, if we are looking for an integral manifold orthogonal to a vector field that is proportional to the gradient of a potential function, such as  $\nabla U(\mathbf{x})$ , then the Theorem of Frobenius gives us the results that we want. Our analysis here is based on the standard literature in differential geometry. See, e.g., [Spi99], Chapter 6; [BG68], Chapter 3; [AM77], Chapter 8; [BC01], Chapter 1; [Lan95], Chapter VI.

Let's consider an  $n - 1$  dimensional *tangent subbundle*,  $E$ , in  $\mathbf{R}^n$  at some point  $\mathbf{x}$  along the integral curve  $\rho(t)$ . We will initially use the Cartesian coordinates from the ambient space  $\mathbf{R}^n$  to define a set of basis vectors for  $E$ , which suggests that one axis should be used to "center" the coordinate system and the other  $n - 1$  axes should be used to specify alternative directions in the vector space. To simplify both the exposition and our later calculations, we will always "center" our coordinate system on  $x^1$  and simply permute the coordinate axes whenever we wish to make a different choice. It will be convenient to establish a special notation for the components of  $\nabla U(\mathbf{x})$  that reflects this convention. Thus we define:

$$\nabla U(\mathbf{x}) = (P_0(\mathbf{x}), P_1(\mathbf{x}), \dots, P_{n-1}(\mathbf{x})),$$

and observe that the term  $P_0(\mathbf{x}) = \partial U(\mathbf{x})/\partial x^1$  will play a special role because of our centering convention. We now define the basis vectors

for  $E$  as follows:

$$\begin{aligned}
\nabla U(\mathbf{x}) &= ( P_0(\mathbf{x}), P_1(\mathbf{x}), P_2(\mathbf{x}), \dots, P_{n-2}(\mathbf{x}), P_{n-1}(\mathbf{x}) ) \\
\mathbf{V}_1(\mathbf{x}) &= ( -P_1(\mathbf{x}), P_0(\mathbf{x}), 0, \dots, 0, 0 ) \\
\mathbf{V}_2(\mathbf{x}) &= ( -P_2(\mathbf{x}), 0, P_0(\mathbf{x}), \dots, 0, 0 ) \\
&\dots \\
\mathbf{V}_{n-2}(\mathbf{x}) &= ( -P_{n-2}(\mathbf{x}), 0, 0, \dots, P_0(\mathbf{x}), 0 ) \\
\mathbf{V}_{n-1}(\mathbf{x}) &= ( -P_{n-1}(\mathbf{x}), 0, 0, \dots, 0, P_0(\mathbf{x}) )
\end{aligned}$$

It is straightforward to verify that  $\nabla U(\mathbf{x})$  is orthogonal to each  $\mathbf{V}_i(\mathbf{x})$ , but we need to analyze the tangent subbundle more carefully to verify the Frobenius integrability conditions.

It is standard in differential geometry to think of a vector field as a differential operator, essentially the *directional derivative* with respect to a given vector  $\mathbf{V}$ . We will write this in shorthand notation as  $\mathbf{V}\partial$ . Let's now consider the vector fields defined by  $\mathbf{V}_i = \mathbf{V}_i(\mathbf{x})/P_0(\mathbf{x})$  and  $\mathbf{V}_j = \mathbf{V}_j(\mathbf{x})/P_0(\mathbf{x})$ , with  $i \neq j$ , and let's compute the *Lie bracket* of  $\mathbf{V}_i\partial$  and  $\mathbf{V}_j\partial$ . By a straightforward (but tedious) calculation, we have:

$$\begin{aligned}
(12) \quad [\mathbf{V}_i\partial, \mathbf{V}_j\partial] &= \mathbf{V}_i\partial \circ \mathbf{V}_j\partial - \mathbf{V}_j\partial \circ \mathbf{V}_i\partial \\
&= \frac{1}{P_0^2} \left( \begin{array}{l} P_0 \left[ \frac{\partial P_i}{\partial x^{j+1}} - \frac{\partial P_j}{\partial x^{i+1}} \right] \\ + P_i \left[ \frac{\partial P_j}{\partial x^1} - \frac{\partial P_0}{\partial x^{j+1}} \right] \\ + P_j \left[ \frac{\partial P_0}{\partial x^{i+1}} - \frac{\partial P_i}{\partial x^1} \right] \end{array} \right) \frac{\partial}{\partial x^1}
\end{aligned}$$

We now substitute the definitions  $P_0 = \partial U(\mathbf{x})/\partial x^1$ ,  $P_i = \partial U(\mathbf{x})/\partial x^{i+1}$  and  $P_j = \partial U(\mathbf{x})/\partial x^{j+1}$ , and we note that the terms in the square brackets vanish identically by virtue of the equality of mixed partial derivatives. Thus  $[\mathbf{V}_i\partial, \mathbf{V}_j\partial] = 0$ , which means that the vector fields  $\mathbf{V}_i\partial$  and  $\mathbf{V}_j\partial$  *commute*.

To formulate the Theorem of Frobenius, we need several definitions. We say that the vector field  $\mathbf{V}\partial$  *belongs to* the tangent subbundle  $E$  if  $\mathbf{V}(\mathbf{x})$  is an element of  $E$  at each point  $\mathbf{x}$  of the domain. Then, if  $[\mathbf{X}\partial, \mathbf{Y}\partial]$  belongs to  $E$  whenever  $\mathbf{X}\partial$  belongs to  $E$  and  $\mathbf{Y}\partial$  belongs to  $E$ , for arbitrary  $\mathbf{X}$  and  $\mathbf{Y}$ , we say that  $E$  is *involutive*. If the tangent subbundle  $E$  can be extended to a full integral manifold, we say that  $E$  is *integrable*. These two concepts are related by the following:

**Theorem 1 (Frobenius).** *A tangent subbundle,  $E$ , is integrable if and only if it is involutive.*

*Proof.* See [BC01], Sections 1.4 and 1.6, and Theorems 5, 6 and 7; [Lan95], Chapter VI, §1 – §4, and Theorems 1.1 and 1.2.  $\square$

We can now show that the tangent subbundle defined above by the basis vectors  $\mathbf{V}_1(\mathbf{x}), \mathbf{V}_2(\mathbf{x}), \dots, \mathbf{V}_{n-1}(\mathbf{x})$ , is involutive, hence integrable.

If  $\mathbf{V}\partial$  and  $\mathbf{W}\partial$  are vector fields and  $f$  and  $g$  are differentiable real-valued functions, we have the following identity for the expansion of Lie brackets:

$$\begin{aligned}
 (13) \quad [f\mathbf{V}\partial, g\mathbf{W}\partial] &= f\mathbf{V}\partial \circ g\mathbf{W}\partial - g\mathbf{W}\partial \circ f\mathbf{V}\partial \\
 &= f(\mathbf{V}\partial g)\mathbf{W}\partial + fg\mathbf{V}\partial \circ \mathbf{W}\partial \\
 &\quad - g(\mathbf{W}\partial f)\mathbf{V}\partial - gf\mathbf{W}\partial \circ \mathbf{V}\partial \\
 &= fg[\mathbf{V}\partial, \mathbf{W}\partial] + f(\mathbf{V}\partial g)\mathbf{W}\partial - g(\mathbf{W}\partial f)\mathbf{V}\partial
 \end{aligned}$$

Now let  $\mathbf{X}\partial$  and  $\mathbf{Y}\partial$  be two arbitrary vector fields that belong to  $E$ , and write each of them in terms of their basis vectors:

$$\begin{aligned}
 \mathbf{X}\partial &= \sum_{i=1}^{n-1} f^i(\mathbf{x})\mathbf{V}_i(\mathbf{x})\partial = \sum_{i=1}^{n-1} f^i(\mathbf{x})P_0(\mathbf{x})\mathbf{V}_i\partial \\
 \mathbf{Y}\partial &= \sum_{j=1}^{n-1} g^j(\mathbf{x})\mathbf{V}_j(\mathbf{x})\partial = \sum_{j=1}^{n-1} g^j(\mathbf{x})P_0(\mathbf{x})\mathbf{V}_j\partial
 \end{aligned}$$

To compute  $[\mathbf{X}\partial, \mathbf{Y}\partial]$ , we apply (13) and use the fact that all terms in the form  $[\mathbf{V}_i\partial, \mathbf{V}_j\partial]$  vanish because of (12), to show that the remaining terms form a linear combination of the basis vectors of  $E$ . Thus  $[\mathbf{X}\partial, \mathbf{Y}\partial]$  belongs to  $E$ , which means that  $E$  is involutive.

Figure 3 shows two views of the integral manifold for the three-dimensional example that was depicted in Figures 1 and 2 in Section 2. The view on the left is based on a coordinate system centered on the  $x$  axis, and it shows several integral curves in the  $xy$  plane (with  $z$  constant) and the  $xz$  plane (with  $y$  constant). The view on the right is based on a coordinate system centered on the  $y$  axis, which was computed by a permutation of the axes resulting in the definition  $P_0(\mathbf{x}) = \partial U(\mathbf{x})/\partial x^2$ . It shows the same integral curves in the  $xy$  plane (with  $z$  constant) along with several new integral curves in the  $yz$  plane (with  $x$  constant). It should be clear that both sets of integral curves are tracing out the same two-dimensional integral manifold. Can this integral manifold be defined without reference to a specific coordinate system?

In [McC18], we reversed the procedure that we have been following here. Theorem 5 in [McC18] asserts the existence of a two-dimensional integral manifold orthogonal to any vector field that is proportional

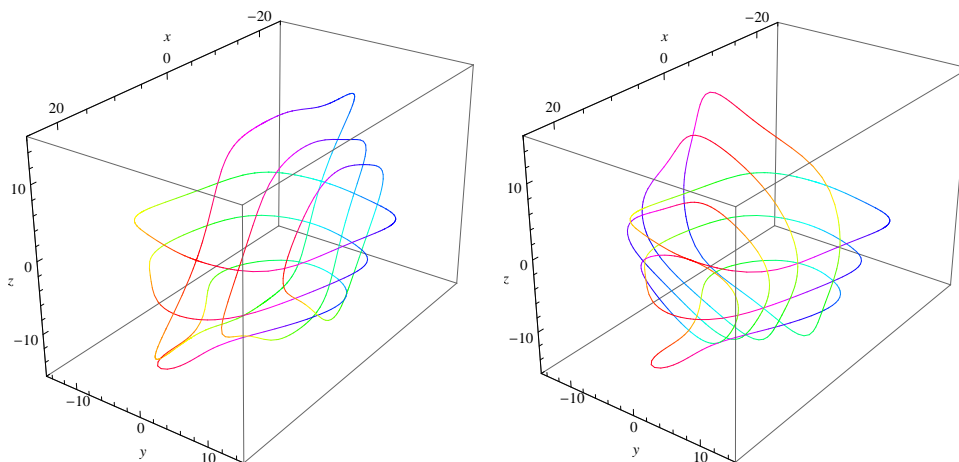


FIGURE 3. An integral manifold with a global coordinate system for the curvilinear Gaussian potential.

to the gradient of a scalar potential function, i.e., any vector field in the form  $N(\mathbf{x})\nabla U(\mathbf{x})$ . The theorem, as stated, makes use of the vector cross product and the “curl,” which is a three-dimensional concept, but it is actually a special case of a general result in  $\mathbf{R}^n$  which follows from the dual version of the Theorem of Frobenius, expressed in terms of differential forms. Thus, if we wanted to, we could develop the theory of our integral manifold in a more “intrinsic” way, without reference to a special coordinate system. We would still have to introduce a coordinate system, of course, when we wanted to do computations, as we did in [McC18], but this would not be our starting point.

We could use either set of integral curves in Figure 3 to define a curvilinear coordinate system on the Frobenius integral manifold, but it would be a *global* coordinate system, since it follows the *global* Cartesian coordinates from the ambient space  $\mathbf{R}^n$ . This would not be particularly useful if we are looking for an “optimal”  $k - 1$  dimensional subspace. But another approach is to use these global vector fields to construct a *local* coordinate system. Any linear combination of  $\mathbf{V}_1(\mathbf{x}), \mathbf{V}_2(\mathbf{x}), \dots, \mathbf{V}_{n-1}(\mathbf{x})$ , could be taken as one of the basis vectors for the tangent subbundle, and we can vary this linear combination as we move around the integral manifold. To implement this idea, it is useful to define a *Riemannian metric* on the integral manifold, and the most natural way to do this is to define a metric tensor on all of  $\mathbf{R}^n$ , using the inner products of  $\nabla U(\mathbf{x}), \mathbf{V}_1(\mathbf{x}), \mathbf{V}_2(\mathbf{x}), \dots$ , and  $\mathbf{V}_{n-1}(\mathbf{x})$ ,

in that order. We thus define:

$$\begin{pmatrix} g_{i,j}(\mathbf{x}) \end{pmatrix} = \begin{pmatrix} |\nabla U|^2 & 0 & 0 & \dots & 0 & 0 \\ 0 & P_0^2 + P_1^2 & P_2 P_1 & \dots & P_{n-2} P_1 & P_{n-1} P_1 \\ 0 & P_1 P_2 & P_0^2 + P_2^2 & \dots & P_{n-2} P_2 & P_{n-1} P_2 \\ \dots & \dots & \dots & \dots & \dots & \dots \\ 0 & P_1 P_{n-2} & P_2 P_{n-2} & \dots & P_0^2 + P_{n-2}^2 & P_{n-1} P_{n-2} \\ 0 & P_1 P_{n-1} & P_2 P_{n-1} & \dots & P_{n-2} P_{n-1} & P_0^2 + P_{n-1}^2 \end{pmatrix}$$

If we want a uniform coordinate notation in place of  $\rho$  and  $\Theta$ , we let  $i$  and  $j$  range over  $0, 1, 2, \dots, n-1$ , and we stipulate that  $u^0 = \rho$ , and  $u^i = \theta^i$ , for  $i = 1, \dots, n-1$ . We will see later why this formula makes sense as a measure of dissimilarity, but for now we will simply adopt it as the definition of our *Riemannian dissimilarity metric*.

What is the purpose of this Riemannian dissimilarity metric? The main application of the metric is to compute *geodesics* on the surface of the integral manifold orthogonal to  $\nabla U(\mathbf{x})$ . Since any linear combination of  $\mathbf{V}_1(\mathbf{x}), \mathbf{V}_2(\mathbf{x}), \dots, \mathbf{V}_{n-1}(\mathbf{x})$ , yields a vector in the tangent subbundle,  $E$ , we can construct vector fields in  $E$  in the form

$$\sum_{i=1}^{n-1} v^i(t) \mathbf{V}_i(\mathbf{x})$$

for arbitrary functions

$$\mathbf{v}(t) = \begin{pmatrix} v^1(t) \\ v^2(t) \\ \dots \\ v^{n-1}(t) \end{pmatrix}$$

For a geodesic, we are looking for a curve  $\gamma(t)$  with values in  $\mathbf{R}^n$  which minimizes the “energy” functional:

$$\frac{1}{2} \int_0^T \mathbf{v}(t)^\top \begin{pmatrix} g_{1,1}(\gamma(t)) & g_{1,2}(\gamma(t)) & \dots & g_{1,n-1}(\gamma(t)) \\ g_{2,1}(\gamma(t)) & g_{2,2}(\gamma(t)) & \dots & g_{2,n-1}(\gamma(t)) \\ \dots & \dots & \dots & \dots \\ g_{n-1,1}(\gamma(t)) & g_{n-1,2}(\gamma(t)) & \dots & g_{n-1,n-1}(\gamma(t)) \end{pmatrix} \mathbf{v}(t) dt$$

subject to the constraint:

$$\gamma'(t) = \sum_{i=1}^{n-1} v^i(t) \mathbf{V}_i(\gamma(t))$$

This variational problem leads to a system of Euler-Lagrange equations for the curves  $\gamma(t)$  and  $\mathbf{v}(t)$ , plus  $n$  Lagrange multipliers, and by the existence and uniqueness theorems for ordinary differential equations, the resulting system will have a solution if we specify the initial conditions  $\gamma(0)$  and  $\mathbf{v}(0)$ .

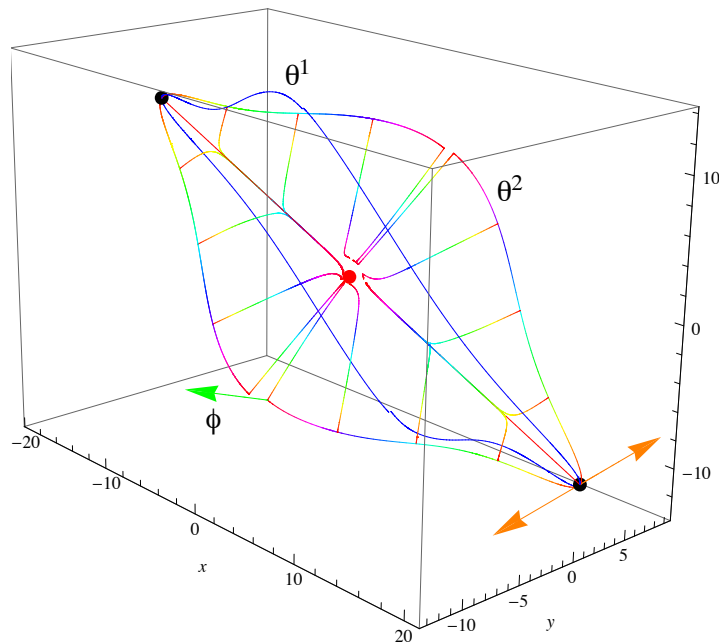


FIGURE 4. The  $\rho$  and  $\Theta$  coordinate curves for the curvilinear Gaussian potential in Figure 1.

Figure 4 shows a local coordinate system for the three-dimensional example that was depicted in Figures 1 and 2 in Section 2, and for which we computed the global coordinate systems in Figure 3. We will use this illustration to explain the necessary calculations, but we are interested in generalizing from three dimensions to  $n$  dimensions, and we will see that the higher dimensional case sometimes requires a slightly different treatment. In either case, there are three steps:

- Step One:

To find a *principal axis* for the  $\rho$  coordinate, we minimize the Riemannian distance,  $g_{i,j}(\mathbf{x})$ , along the drift vector.

- Step Two:

To choose the *principal directions* for the  $\theta^1, \theta^2, \dots, \theta^{k-1}$  coordinates, we diagonalize the Riemannian matrix,  $(g_{i,j}(\mathbf{x}))$ , at a fixed point,  $\mathbf{x}_0$ , along the principal axis.

- Step Three:

To compute the  $\Theta$  *coordinate curves*, we follow the geodesics of the Riemannian metric,  $g_{i,j}(\mathbf{x}_0)$ , in each of the  $k - 1$  principal directions.

It turns out that Step Two requires the greatest modifications in the higher dimensional case, so we will defer that discussion and consider Step One and Step Three first.

In Step One, we compute the *principal axes*, which are the curves in Figure 4 that extend from the black dots to the red dot. One way to do this is to find a point at a fixed Euclidean distance from the origin for which the integral curve,  $\rho(t)$ , as defined in Equation (10) or (11), has minimal Riemannian length to the origin. However, if  $|\nabla U(\mathbf{x})|$  is monotonic, we obtain approximately the same results (i.e., within the accuracy of our numerical approximations) by simply minimizing  $|\nabla U(\mathbf{x})|^2$  on a sphere at a constant distance from the origin. For example, to find the black dot in the lower right corner of Figure 4, we first minimize  $|\nabla U(x, y, z)|^2$  on the sphere  $x^2 + y^2 + z^2 = 500$  to locate a point and a curve,  $\rho(t)$ , with Riemannian length 6.30873. We then search within the neighborhood of this solution to find a point and a curve with a slightly smaller Riemannian length: 6.30863. In Figure 4, we have chosen the latter solution, but in an  $n$ -dimensional space, the second solution is usually too complex, computationally, and we therefore stick with the simple minimization of  $|\nabla U(\mathbf{x})|^2$ .

Let's now jump ahead to Step Three. Setting  $\gamma(0) = \mathbf{x}_0$ , which is the black dot on the principal axis in Figure 4, and setting  $\mathbf{v}(0)$  equal to one of the principal directions from Step Two, we solve the Euler-Lagrange equations. The results are the *coordinate curves*  $\theta^1$  and  $\theta^2$  in Figure 4. These curves have interesting geometric properties. Since they are geodesics on the surface of the Frobenius integral manifold, they are always a constant Riemannian distance from the origin. Note that we have drawn several  $\rho$  coordinate curves in Figure 4 from the  $\theta^2$  curve to the origin. The Riemannian length of these curves is approximately 6.30863, even though their Euclidean length varies considerably. On the other hand, the Riemannian distance along the  $\theta^1$  and  $\theta^2$  curves is the same as the Euclidean distance, and we can therefore use the

Riemannian/Euclidean arc length to parametrize these curves, just as we have done with the  $\rho$  coordinate curves.

In practice, when we try to solve the Euler-Lagrange equations in Step Three of our procedure, we often encounter a singularity, as the value of  $P_0(\mathbf{x})$  approaches zero. The solution is to shift the “center” of our coordinate system to a different coordinate axis, and then continue the computation with a new value for  $P_0(\mathbf{x})$ . To validate this solution, though, we need to show that our definition of the Riemannian metric,  $g_{i,j}(\mathbf{x})$ , is independent of our choice of a “centered” coordinate axis. For the three-dimensional case, the proof appears at the end of Section 4 in [McC18], and the proof for  $n$  dimensions is a straightforward generalization. Let  $\mathbf{u}(\mathbf{x})$  denote a  $\rho, \Theta$ , coordinate system centered on the  $x^1$  axis, and let  $\bar{\mathbf{u}}(\mathbf{x})$  denote a  $\rho, \Theta$ , coordinate system centered on the axis  $x^p$ , for some  $p \neq 1$ . (For example, look at the second image in Figure 3, in which  $p = 2$  and the centered coordinate axis is  $x^2$ .) The Jacobian matrix of the coordinate transformation from  $\bar{\mathbf{u}}(\mathbf{x})$  to  $\mathbf{u}(\mathbf{x})$  can be computed as follows:

$$\left( \frac{\partial u^i}{\partial \bar{u}^k} \right) = \left( \frac{\partial x^j}{\partial u^i} \right)^{-1} \left( \frac{\partial x^j}{\partial \bar{u}^k} \right)$$

Now let  $g_{i,j}(\mathbf{x})$  and  $\bar{g}_{k,l}(\mathbf{x})$  denote the dissimilarity metric based on the  $u^i$  and  $\bar{u}^k$  coordinates, respectively. We can verify by a straightforward computation (compare the three-dimensional example in [McC18]) that

$$\bar{g}_{k,l}(\mathbf{x}) = \sum_{i,j=1}^{n-1} \frac{\partial u^i}{\partial \bar{u}^k} g_{i,j}(\mathbf{x}) \frac{\partial u^j}{\partial \bar{u}^l}$$

But this is just an instantiation of the transformation law for a type (0,2) tensor. Thus, on an integral manifold of dimension  $n - 1$ , for a fixed  $\rho$ , the dissimilarity metric,  $g_{i,j}(\mathbf{x})$ , is independent of the global coordinate system used to define it.

Once we have computed the geodesic coordinate curves  $\theta^1, \theta^2, \dots, \theta^{k-1}$ , all of which emanate from  $\mathbf{x}_0$ , we also need to construct a system of *transverse* coordinate curves, which can emanate from any point,  $\mathbf{x}$ , on the integral manifold. For this purpose, we define the following *flows*:

$$(14) \quad \vec{\theta}_t(\mathbf{x}) = \hat{\theta}_{\mathbf{x}}(t) = \mathbf{x} + \int_0^t \sum_{i=1}^{n-1} v_{\theta}^i(s) \mathbf{V}_i(\hat{\theta}_{\mathbf{x}}(s)) ds$$

Here,  $\hat{\theta}_{\mathbf{x}}(t)$  is an integral curve starting at  $\mathbf{x}$ , as in (11), and it has an equivalent definition by a differential equation, as in (10). We have

one such flow equation for each geodesic,  $\theta^1, \theta^2, \dots, \theta^{k-1}$ , computed in Step Three, in which the coefficient vectors,  $\mathbf{v}_{\theta^1}(s), \mathbf{v}_{\theta^2}(s), \dots, \mathbf{v}_{\theta^{k-1}}(s)$ , are the functions,  $\mathbf{v}(t)$ , that were computed at the same time. When  $\mathbf{x} = \mathbf{x}_0$ , of course, the integral curve in Equation (14) coincides with the original geodesic coordinate curve. In the  $n$ -dimensional case, we usually apply Equation (14) in a fixed order to a sequence of coordinates to specify a point on the integral manifold. Thus, we start with the flow  $\vec{\theta}_t^1(\mathbf{x}_0)$  and follow it for a distance  $t_1$  to the point  $\mathbf{x}_1$ ; we then follow the flow  $\vec{\theta}_t^2(\mathbf{x}_1)$  for a distance  $t_2$  to the point  $\mathbf{x}_2$ ; and so on. In the three-dimensional case, as shown in Figure 4, it is convenient to define an additional geodesic coordinate curve,  $\phi$ , which is orthogonal to both  $\theta^1$  and  $\theta^2$ . We then have three flows,  $\vec{\theta}_t^1(\mathbf{x}), \vec{\theta}_t^2(\mathbf{x})$ , and  $\vec{\phi}_t(\mathbf{x})$ , and we can compose them either as  $\vec{\phi}_s \circ \vec{\theta}_t^1(\mathbf{x}_0)$  or as  $\vec{\phi}_s \circ \vec{\theta}_t^2(\mathbf{x}_0)$ . (We will see later that this choice leads to an interesting comparative analysis.) Whatever choices we make, though, we want to make sure that our coordinate system covers the entire integral manifold.

Let's now return to Step Two, where we encounter a surprising mathematical fact. When we diagonalize the Riemannian matrix,  $(g_{i,j}(\mathbf{x}))$ , in  $n$  dimensions, we find only two distinct eigenvalues. The largest eigenvalue has multiplicity 2:  $\lambda_0 = \lambda_1 = |\nabla U|^2$ , with corresponding eigenvectors:

$$\xi_0 = \begin{pmatrix} 1 \\ 0 \\ 0 \\ \dots \\ 0 \\ 0 \end{pmatrix} \quad \text{and} \quad \xi_1 = \begin{pmatrix} 0 \\ P_1 \\ P_2 \\ \dots \\ P_{n-2} \\ P_{n-1} \end{pmatrix}$$

The smallest eigenvalue has multiplicity  $n-2$ :  $\lambda_2 = \lambda_3 = \dots = \lambda_{n-2} = \lambda_{n-1} = P_0^2$ , with corresponding eigenvectors  $\xi_2, \xi_3, \dots, \xi_{n-2}, \xi_{n-1}$ , as follows:

$$\begin{pmatrix} 0 \\ -P_2 \\ P_1 \\ 0 \\ \dots \\ 0 \\ 0 \end{pmatrix}, \begin{pmatrix} 0 \\ -P_3 \\ 0 \\ P_1 \\ \dots \\ 0 \\ 0 \end{pmatrix}, \dots, \begin{pmatrix} 0 \\ -P_{n-2} \\ 0 \\ 0 \\ \dots \\ P_1 \\ 0 \end{pmatrix}, \begin{pmatrix} 0 \\ -P_{n-1} \\ 0 \\ 0 \\ \dots \\ 0 \\ P_1 \end{pmatrix}$$

This means that the three-dimensional case is special, since it only has three eigenvectors:

$$\xi_0 = \begin{pmatrix} 1 \\ 0 \\ 0 \end{pmatrix}, \quad \xi_1 = \begin{pmatrix} 0 \\ P_1 \\ P_2 \end{pmatrix}, \quad \xi_2 = \begin{pmatrix} 0 \\ -P_2 \\ P_1 \end{pmatrix}$$

See Section 4 of [McC18]. We should think of these  $\{\xi_i\}$  as *infinitesimal* eigenvectors. They tell us the maximal and minimal *initial* directions for the integrand of the energy functional:

$$(15) \quad \xi_1^\top (g_{i,j}) \xi_1 = \xi_1^\top (\lambda_1 \xi_1) = \lambda_1 |\xi_1|^2 = |\nabla U|^2 |\xi_1|^2$$

$$(16) \quad \xi_2^\top (g_{i,j}) \xi_2 = \xi_2^\top (\lambda_2 \xi_2) = \lambda_2 |\xi_2|^2 = P_0^2 |\xi_2|^2$$

However, we are primarily interested in minimizing geodesic curves over *finite* distances, and there is no guarantee that minimizing the initial directions of the geodesics in the Euler-Lagrange equations will achieve this result.

Our solution to this problem in [McC18] is to rotate the infinitesimal eigenvectors around  $\mathbf{x}_0$ , and then compute the Riemannian/Euclidean distances along each rotated geodesic, up to some specified point, for example, up to the Euclidean angle  $\pi/2$  from the origin, so that we can determine the *global* minimum or maximum. In Figure 4, the orange arrows depict the minimal infinitesimal eigenvector,  $\xi_2$ , in the positive  $y$ -direction and the negative  $y$ -direction, respectively. But the minimal geodesics over a finite distance, labelled as  $\theta^2$ , were obtained by a counter-clockwise rotation through the angle  $\alpha = 0.952169$  in the positive direction, and the angle  $\alpha = 1.12681$  in the negative direction. For the maximal infinitesimal eigenvector,  $\xi_1$ , the maximal geodesics over a finite distance, labelled as  $\theta^1$ , were obtained by a counter-clockwise rotation through the angle  $\alpha = 0.114166$ . See Section 5.2 of [McC18] for the detailed calculations.

Now look at Figure 5. This figure includes the same view of the  $\theta^1$  and  $\theta^2$  coordinate curves as in Figure 4. It also includes 1000 data points generated according to the curvilinear Gaussian probability distribution from Figure 1, and projected along the  $\rho$  coordinate curve to the Frobenius integral manifold. Qualitatively, the density of the data is higher near the  $\theta^2$  coordinate curve than it is near the  $\theta^1$  coordinate curve, and we can quantify this observation by computing a value for the “reconstruction error” adapted to our curvilinear coordinate system. For this purpose, we use the geodesic coordinate curve,  $\phi$ , which is aligned with the green arrow in Figure 4, and its flow,  $\vec{\phi}_s(\mathbf{x})$ . We want to compare two curvilinear coordinate systems for each data

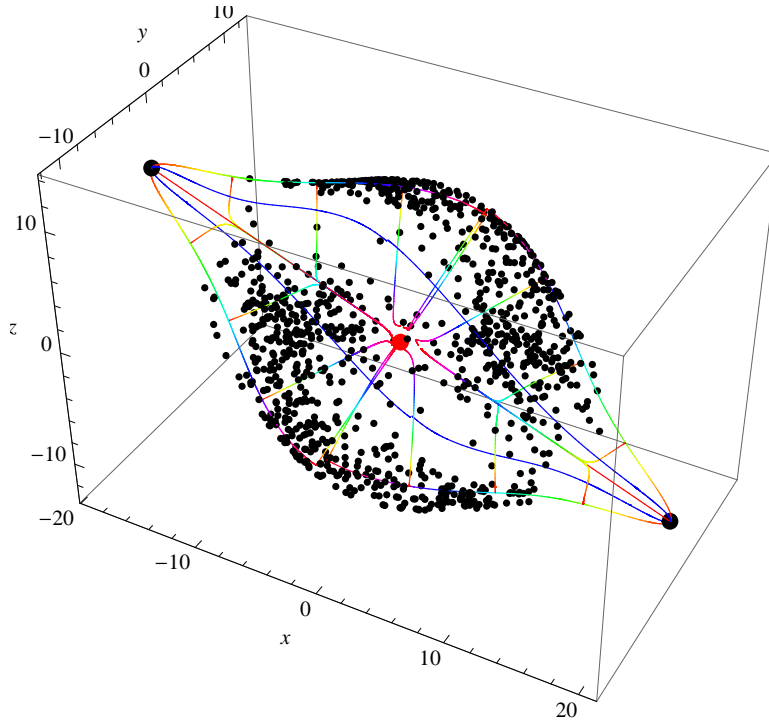


FIGURE 5. Projecting data points from the curvilinear Gaussian potential along the  $\rho$  coordinate curves to the Frobenius integral manifold.

point:  $(\rho, \theta^1, \phi)$ , which is defined by following the flow  $\vec{\phi}_s \circ \vec{\theta}_t^1(\mathbf{x}_0)$  on the integral manifold, and  $(\rho, \theta^2, \phi)$ , which is defined by following the flow  $\vec{\phi}_s \circ \vec{\theta}_t^2(\mathbf{x}_0)$ . What happens when we drop the  $\phi$  coordinate, in each case? We can measure the “reconstruction error” by computing the Euclidean distance along the flow,  $\vec{\phi}_s$ , and scaling this value down, proportionately, by the position of the data point along the  $\rho$  coordinate curve. We can then compute the *root-mean-squared* (RMS) reconstruction error for the 1000 data points in each coordinate system. It turns out that the RMS error for the truncation from  $(\rho, \theta^1, \phi)$  to  $(\rho, \theta^1)$  is 5.9431, and the RMS error for the truncation from  $(\rho, \theta^2, \phi)$  to  $(\rho, \theta^2)$  is 4.82787. Thus, according to this criteria, the “optimal” lower dimensional encoding is  $(\rho, \theta^2)$ . See Section 5.2 of [McC18] again for the detailed calculations.

Recall that the  $\theta^2$  coordinate curve was derived from the minimal infinitesimal eigenvector,  $\xi_2$ , by rotating it a small amount in order to minimize the length of the geodesic over a finite Euclidean angle. This

is a purely geometric calculation. However, our analysis of the reconstruction error shows that projection of the data onto the  $\theta^2$  subspace has better statistical properties than projection onto the  $\theta^1$  subspace. Thus the link between the geometric model and the probabilistic model has computational implications. Here is an informal explanation:

... The geodesic curves on the Frobenius integral manifold tend to follow the *modes* of the probability distribution. First, the origin of the coordinate system is a point at which  $\nabla U(\mathbf{x}) = (0, 0, 0)$ , which maximizes the probability density. Second, to compute the principal axis, we are looking for a point with a minimal Riemannian distance for a fixed Euclidean distance, or a maximal Euclidean distance for a fixed Riemannian distance. Under either formulation, this is an axis that maximizes probability. Third, for the directional coordinates, we are looking for a geodesic curve on the Frobenius integral manifold that covers a minimal Riemannian distance for a fixed angular Euclidean distance, or a maximal angular Euclidean distance for a fixed Riemannian distance. Under either formulation, again, this is a curve that maximizes probability. Thus, in general, we are *minimizing* dissimilarity and *maximizing* probability. This is the primary intuition behind the claim that we are constructing an “optimal” lower dimensional coordinate system.

See [McC18], Section 5.2.

For a more formal analysis of the link between the geometric model and the probabilistic model, and a possible mathematical explanation of why the clustering of data points in Figure 5 occurs, see Section 6 of [McC18].

What do we need to do to extend these ideas to  $n$  dimensions? Rotating the eigenvectors to find the optimal initial directions is not likely to work in  $n$  dimensions. In Figure 4, we rotated the minimal infinitesimal eigenvector in a two-dimensional plane, and we were able to compute and compare the geodesics under each rotation. These rotations and calculations would not be feasible in an  $n - 1$  dimensional hyperplane. However, the more important principle suggested by this example is that we should search among a set of candidates for a *minimal* geodesic over a *finite* distance. In  $n$  dimensions, we can apply this principle to the set of minimal infinitesimal eigenvectors. First, note that any linear combination of the eigenvectors,  $\xi_2, \xi_3, \dots, \xi_{n-2}, \xi_{n-1}$ , is also an eigenvector associated with the eigenvalue  $\lambda_2 = P_0^2$ . We can

therefore define new eigenvectors in the form:

$$(17) \quad \zeta = c_2 \xi_2 + c_3 \xi_3 + \dots + c_{n-2} \xi_{n-2} + c_{n-1} \xi_{n-1},$$

where the coefficients,  $c_i$ , are either  $+1$  or  $-1$ . (There are  $2^{n-2}$  sequences of such coefficients, of course, but in practice we can generate a large subset randomly.) If we evaluate the integrand of the energy functional on these new eigenvectors, we have:

$$(18) \quad \zeta^\top (g_{i,j}) \zeta = \zeta^\top (\lambda_2 \zeta) = \lambda_2 |\zeta|^2 = P_0^2 |\zeta|^2$$

Now, order the eigenvectors,  $\{\zeta\}$ , by their norms and apply the Gram-Schmidt orthogonalization procedure to a subsequence of length  $n - 2$  or more. We will then have an orthonormal basis for the  $n - 2$  dimensional tangent subbundle at  $\mathbf{x}_0$ , in which each basis vector represents a minimal initial direction for the solution of the Euler-Lagrange equations, by (18). Finally, from among these solutions, we simply select the  $k$  coordinate curves which have the minimal Riemannian length over a fixed angular Euclidean distance. We will see how this works, using real data, in Sections 6 and 7, *infra*.

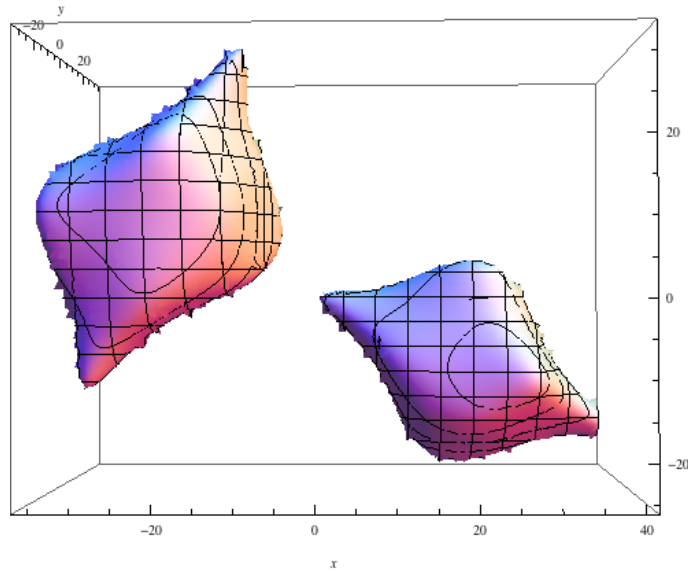


FIGURE 6. A mixture of two curvilinear Gaussians, translated and rotated.

We will also analyze in Sections 6 and 7 a representation of *clusters*, using real data. The basic idea is illustrated for the three-dimensional case in Figure 6, which shows two copies of the curvilinear Gaussian

potential from Figure 1. One copy has been translated from  $(0, 0, 0)$  to  $(20, 20, -10)$ . The other copy has been translated from  $(0, 0, 0)$  to  $(-20, -20, 10)$  and rotated by  $\pi/2$  around a line parallel to the  $y$ -axis. But the probability density is a *mixture*. If  $U_1(\mathbf{x})$  is the potential function for the first copy and  $U_2(\mathbf{x})$  is the potential function for the second copy, then the invariant probability density is given by:

$$e^{2U(\mathbf{x})} \simeq p_1 e^{2U_1(\mathbf{x})} + p_2 e^{2U_2(\mathbf{x})},$$

modulo an appropriate normalization factor. The advantage of this representation lies in the fact that our calculations for each copy will be almost independent of each other. Observe that the effective potential function for the mixture will be:

$$U(\mathbf{x}) \simeq \frac{1}{2} \log(p_1 e^{2U_1(\mathbf{x})} + p_2 e^{2U_2(\mathbf{x})})$$

Thus the gradient of  $U(\mathbf{x})$  in a neighborhood of  $(20, 20, -10)$  will be almost identical to the gradient of  $U_1(\mathbf{x})$  computed by itself, and the gradient of  $U(\mathbf{x})$  in a neighborhood of  $(-20, -20, 10)$  will be almost identical to the gradient of  $U_2(\mathbf{x})$  computed by itself. Or, in terms of our dissimilarity metric, the two clusters in Figure 6 will be exponentially far apart.

#### 4. HOW TO ESTIMATE $\nabla U(\mathbf{x})$ FROM SAMPLE DATA.

To apply the theory of differential similarity to real data, we need to estimate the quantities that appear in the equations for the  $\rho$ ,  $\Theta$ , coordinate system. Fortunately, this is not hard to do: We will borrow a technique from the literature on the *mean shift algorithm* [FH75] [Che95] [CM02].

Consider a *kernel density estimator* with a Gaussian kernel:

$$K(\mathbf{s}_k, \mathbf{x}) = \exp(-\beta \|\mathbf{s}_k - \mathbf{x}\|^2)$$

in which  $\mathbf{s}_k$  is a sample data point and  $\beta$  is a smoothing parameter. We can approximate a probability density by taking the average over these kernels:

$$\hat{\mu}(\mathbf{x}) = \frac{1}{n} \sum_{k=1}^n K(\mathbf{s}_k, \mathbf{x})$$

Now recall that  $\nabla U(\mathbf{x})$  is the *gradient* of the *log* of the stationary probability density in our theory. So we can differentiate explicitly:

$$(19) \quad \frac{\partial}{\partial x^j} \log \hat{\mu}(\mathbf{x}) = 2\beta \left[ \frac{\sum_{k=1}^n K(\mathbf{s}_k, \mathbf{x}) s_k^j}{\sum_{k=1}^n K(\mathbf{s}_k, \mathbf{x})} - x^j \right]$$

to obtain an estimate for  $\nabla U(\mathbf{x})$ .

```

pkernel[p_, β_] := Exp[-β * (p.p)]

pmeanshift[x_, β_, Sample_] :=
  2 * β *
  (Fold[ Plus[#1, pkernel[#2 - x, β] * #2] &, 0, Sample] /
   Fold[ Plus[#1, pkernel[#2 - x, β]] &, 0, Sample] - x)

pgradascent[xstart_, β_, Sample_] :=
  Module[{x = xstart, ms = pmeanshift[xstart, β, Sample]},
    (While[byteArray7X7[ms] != zeroArray,
      (x = x + ms; ms = pmeanshift[x, β, Sample])]; Return[x])]

```

FIGURE 7. The mean shift algorithm.

Figure 7 shows an example of *Mathematica* code that implements Equation (19) and calls it `pmeanshift`. The expression “mean shift” refers to the fact that the first term inside the square brackets computes the weighted mean of the sample data points,  $\{\mathbf{s}_k\}$ , around the point  $\mathbf{x}$ , and the second term subtracts  $\mathbf{x}$  from this value to define a shift. This function is typically used in a gradient ascent algorithm, such as `pgradascent`. (In Figure 7, `byteArray7X7` and `zeroArray` are tailored to the examples in Sections 6 and 7, *infra*.) In this case, the gradient ascent algorithm will find the *mode* of the probability density,  $\hat{\mu}(\mathbf{x})$ , for a given `Sample`. It is often applied iteratively: Choose a sample around  $\mathbf{x}$ , ascend to the mode of the probability density to find a new  $\mathbf{x}$ , choose another sample, and repeat.

We can certainly apply the code in Figure 7 to find the origin of an admissible coordinate system in our theory, and we will see an example of this kind of an application in Section 6. However, Equation (19) has a much broader application than this, because every quantity that enters into the definition of the  $\rho$  coordinates and the  $\Theta$  coordinates depends on  $\nabla U(\mathbf{x})$ . We will actually modify (19) slightly to simplify these calculations. The quantity  $\sum_{k=1}^n K(\mathbf{s}_k, \mathbf{x})$  in the denominator of the first term is a normalization factor, and we can multiply the formula by this factor (and divide out the factor  $2\beta$ ) to write down an equation for the gradient without normalization:

$$\text{DU}_j(\mathbf{x}) = \sum_{k=1}^n K(\mathbf{s}_k, \mathbf{x}) s_k^j - x^j \sum_{k=1}^n K(\mathbf{s}_k, \mathbf{x})$$

The second derivatives are now much easier to compute:

$$\frac{\partial}{\partial x^i} \text{DU}_j(\mathbf{x}) = 2\beta \sum_{k=1}^n K(\mathbf{s}_k, \mathbf{x})(x^i - s_k^i)(x^j - s_k^j) - \delta_{i,j} \sum_{k=1}^n K(\mathbf{s}_k, \mathbf{x}),$$

where  $\delta_{i,j}$  is the Kronecker delta function. These modifications will not alter the specification of our coordinate system, for two reasons: (1) the definition of the  $\rho$  coordinate in Equations (10) and (11) is already normalized, so the factor  $\sum_{k=1}^n K(\mathbf{s}_k, \mathbf{x})$  would cancel out; and (2) the basis vectors  $\{\mathbf{V}_i(\mathbf{x})\}$  can be divided by  $P_0(\mathbf{x})$  without affecting the Frobenius integral manifold, so again the factor  $\sum_{k=1}^n K(\mathbf{s}_k, \mathbf{x})$  would cancel out. The code for `DUjF` and `DiDUjF` is shown in Figure 8. The variables `beta` and `SamplePoints` are intended to be defined externally, and the vector variable `VexpK` is expected to be instantiated by the kernel function `VkernelF`.

```
VkernelF[x_?VectorQ] := Map[pkernel[x - #, beta] &, SamplePoints]
```

```
DUjF[x_?VectorQ, VexpK_?VectorQ] :=  
VexpK.SamplePoints - Total[VexpK] * x
```

```
XSkjF[i_, x_?VectorQ] :=  
Table[(x[[i]] - SamplePoints[[k, i]]) * (x[[j]] - SamplePoints[[k, j]]),  
{k, Nsamples}, {j, Ndims}]
```

```
DiDUjF[i_, x_?VectorQ, VexpK_?VectorQ] :=  
2 * beta * (VexpK.XSkjF[i, x]) - Total[VexpK] * IdentityMatrix[Ndims][[i]]
```

FIGURE 8. The gradient (without normalization) and its derivatives.

## 5. COMPUTING THE GEODESIC COORDINATE CURVES.

The main data structures in our theory are defined in Figure 9. But the only data structure needed to write down the Euler-Lagrange equations is the gradient:  $\nabla U(\mathbf{x}) = (P_0(\mathbf{x}), P_1(\mathbf{x}), \dots, P_{n-1}(\mathbf{x}))$ . Here are

```

PNK[x_?VectorQ] := DUjF[x, VkernelF[x]]

VNK[x_?VectorQ] :=
With[{PN = PNK[x]},
Prepend[Table[SparseArray[[1, i + 1] → {-PN[[i + 1]], PN[[1]]}], Ndims],
{i, Ndims - 1}], PN]]

GijNK[x_?VectorQ] :=
With[{VN = VNK[x]},
With[
{m = Table[If[i > j, N[VN[[i]].VN[[j]]], 0], {i, Ndims}, {j, Ndims}}],
m + DiagonalMatrix[Table[N[VN[[k]].VN[[k]]], {k, Ndims}}] +
Transpose[m]]]

```

FIGURE 9. The gradient:  $P_0(\mathbf{x}), P_1(\mathbf{x}), \dots, P_{n-1}(\mathbf{x})$ , the basis vectors:  $\{\mathbf{V}_i(\mathbf{x})\}$ , and the Riemannian dissimilarity metric:  $(g_{i,j}(\mathbf{x}))$ .

the Euler-Lagrange equations:

$$\lambda'_{i-1}(t) = \left( P_0[\mathbf{x}(t)] \sum_{j=1}^{d-1} (v^j)^2(t) - \sum_{j=1}^{d-1} v^j(t) \lambda_j(t) \right) \frac{\partial P_0}{\partial x^i}[\mathbf{x}(t)] + \left( \sum_{j=1}^{d-1} P_j[\mathbf{x}(t)] v^j(t) + \lambda_0(t) \right) \sum_{j=1}^{d-1} \frac{\partial P_j}{\partial x^i}[\mathbf{x}(t)] v^j(t),$$

for  $i = 1, \dots, d$

$$v^i(t) = \frac{1}{P_0[\mathbf{x}(t)]} \left( \lambda_i(t) - P_i[\mathbf{x}(t)] \frac{\sum_{j=0}^{d-1} P_j[\mathbf{x}(t)] \lambda_j(t)}{\sum_{j=0}^{d-1} P_j^2[\mathbf{x}(t)]} \right),$$

for  $i = 1, \dots, d-1$

$$(x^1)'(t) = - \sum_{j=1}^{d-1} P_j[\mathbf{x}(t)] v^j(t)$$

$$(x^i)'(t) = P_0[\mathbf{x}(t)] v^{i-1}(t), \text{ for } i = 2, \dots, d$$

This is a system of ordinary differential equations for  $\mathbf{x}(t)$  and for the Lagrange multipliers,  $\{\lambda_i(t)\}$ , plus a system of algebraic equations for  $\mathbf{v}(t)$ , in which  $d$  is the dimensionality of the space. In addition, we have to include the set of kernel equations, which enter into the definition of

the gradient. So this is a very large system of equations, approximately  $3 * \text{Ndims} + \text{Nsamples}$ .

```

EulerGroupAi[i_, x_?VectorQ, Vbasis_?VectorQ, LambdaK_?VectorQ,
VexpK_?VectorQ] :=
With[{PN = DUJF[x, VexpK], DPN = DiDUJF[i, x, VexpK]},
DPN[[1]] *
(PN[[1]] * (Vbasis.Vbasis) - Vbasis.Take[LambdaK, -Ndims + 1]) +
(Take[PN, -Ndims + 1].Vbasis + LambdaK[[1]])
(Take[DPN, -Ndims + 1].Vbasis)]

EulerGroupBi[i_, x_?VectorQ, LambdaK_?VectorQ, VexpK_?VectorQ] :=
With[{PN = DUJF[x, VexpK]},
(LambdaK[[i + 1]] - PN[[i + 1]) ((PN.LambdaK) / (PN.PN)) / PN[[1]]]

EulerGroupCi[1, x_?VectorQ, Vbasis_?VectorQ, VexpK_?VectorQ] :=
With[{PN = DUJF[x, VexpK]}, -(Take[PN, -Ndims + 1].Vbasis)]

EulerGroupCi[i_, x_?VectorQ, Vbasis_?VectorQ, VexpK_?VectorQ] :=
If[i > 1, With[{PN = DUJF[x, VexpK]}, PN[[1]] Vbasis[[i - 1]]]]

```

FIGURE 10. The Euler-Lagrange equations in *Mathematica*.

Figure 10 shows the *Mathematica* code for the right-hand sides of the Euler-Lagrange equations, in three groups. Tracing this code back from Figure 10 to Figure 8, it is easy to verify that everything depends on the set of `SamplePoints` and the constant  $\beta$ . Thus we should be able to apply this code to a real dataset. We will see how this works in Section 6 on the MNIST Dataset, and in Section 7 on the CIFAR-10 Dataset.

## 6. EXAMPLE: $7 \times 7$ PATCHES IN THE MNIST DATASET.

Figure 11 displays an architecture for deep learning on the MNIST Dataset [LBBH98], based on several examples in the recent literature [Ran09] [Coa12]. The process starts in the lower-left corner and follows the arrows to the upper-right corner. The first step is to scan and randomly sample the 60,000  $28 \times 28$  images to extract a collection of  $7 \times 7$  “patches” from each one. Choosing a sampling rate of 10 scans per image, which is approximately 2%, we end up with 600,000 patches, each one represented as a point in a 49-dimensional space. The original image intensity at each pixel is represented by an integer in the range  $[0, 255]$ , but we have scaled these values down to a real number in the range  $[0, 1]$ . Thus the greatest distance between any two points in our 49-dimensional hypercube is  $\sqrt{49} = 7.0$ . We will be using the theory

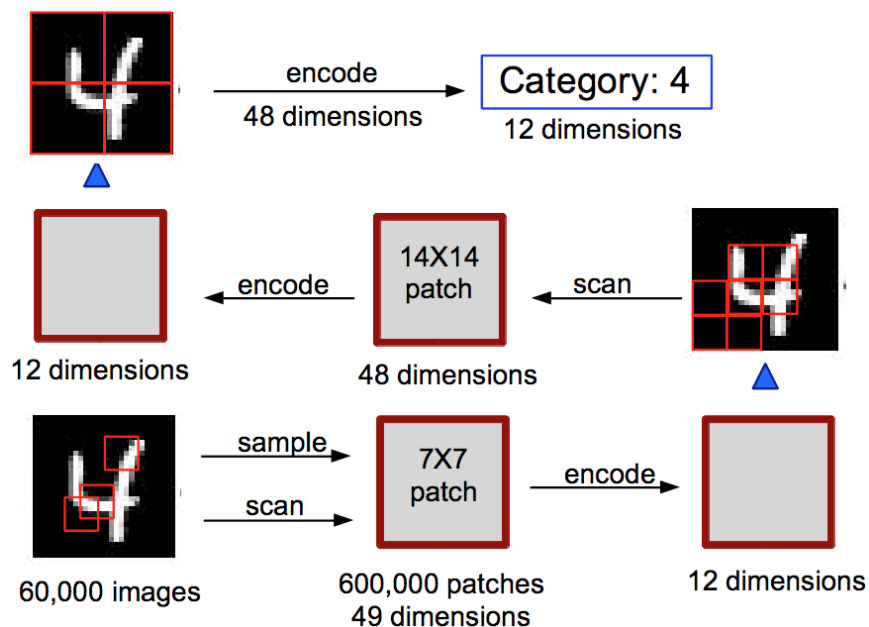


FIGURE 11. An architecture for deep learning on the MNIST Dataset.

of differential similarity, in this section of the paper, to reduce the dimensionality of the space to 12 dimensions, as shown in the lower-right corner of Figure 11. Note that the process continues upwards (following the blue arrow) by assembling four adjacent  $7 \times 7$  patches into a  $2 \times 2$  matrix and then resampling the image using the larger  $14 \times 14$  patch, but we will not pursue this analysis in the present paper. We are thus looking only at the first step in the process, which is an example of the classical problem of *unsupervised feature learning*.

There are several parameters that control the behavior of the algorithms defined in Sections 4 and 5. The smoothing parameter,  $\beta$ , can be set to different values in different circumstances. (In the traditional notation for a Gaussian,  $\beta = 1/2\sigma^2$ .) We have experimented with a range of values, but we have found that the two values,  $\beta = 1/8$  (or  $\sigma = 2.0$ ) and  $\beta = 1$  (or  $\sigma = 0.707107$ ), are sufficient for most purposes. A typical strategy is to run a computation with  $\beta = 1/8$ , for a coarse approximation, and then to refine the result by running the computation again with  $\beta = 1$ . Another parameter is the variable `SamplePoints`. *Mathematica* provides a function called `Nearest` which, when applied to a large dataset, returns a `NearestFunction` which maintains an efficient data structure that can find the  $n$  points that are the nearest to any specified point in the dataset. Again, we

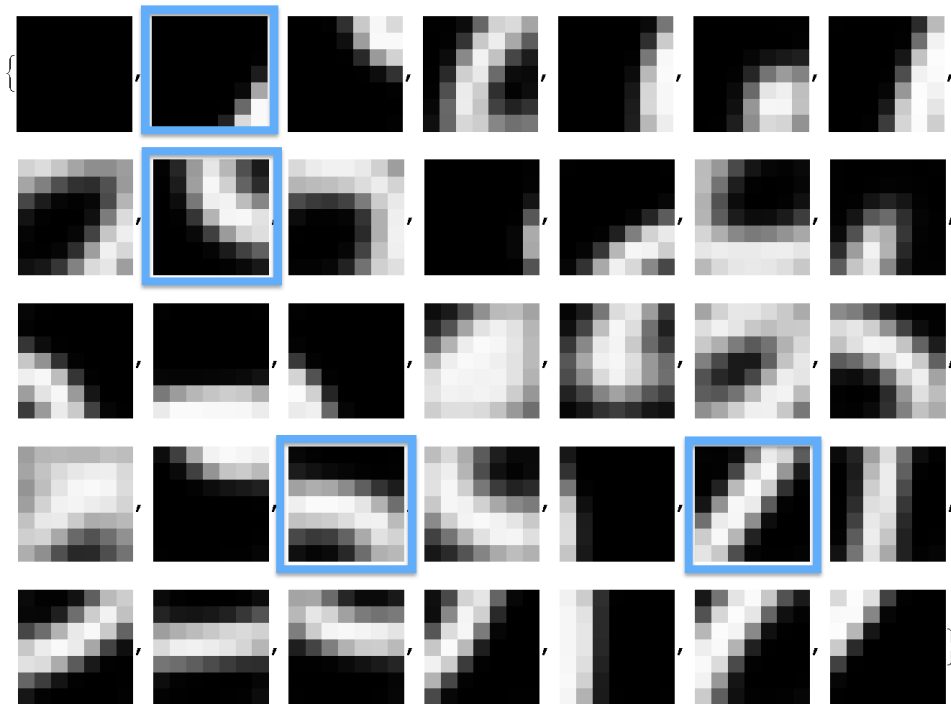


FIGURE 12. 35 prototypes for the 600,000  $7 \times 7$  patches in the MNIST Dataset.

have experimented with several values of  $n$ , but we have found that a *Data Sphere* of 32,000 points around each prototype yields good results. Within each Data Sphere, we draw two random 800 point samples and use these as inputs to the algorithms in Sections 4 and 5. A typical strategy is to run the computations separately on each 800 point sample, and if the results are qualitatively the same and quantitatively within the range that we would expect from random sampling, then we run a final computation on the union of the two samples. Note that a 1600 point sample is 5% of a 32,000 point Data Sphere.

In addition to the definition of the Data Sphere, it is also useful to define a *Coordinate Sphere* for each prototype. Recall that the principal axis is defined by a point at a fixed Euclidean distance from the origin that has a minimal Riemannian distance to the origin, as measured along the  $\rho$  coordinate curve. The fixed Euclidean distance gives us a sphere, of course, and it is reasonable again to think of the size of this sphere in terms of the number of data points it contains. Combined with a 32,000 point Data Sphere, we have found that an 8,000 point Coordinate Sphere yields good results.

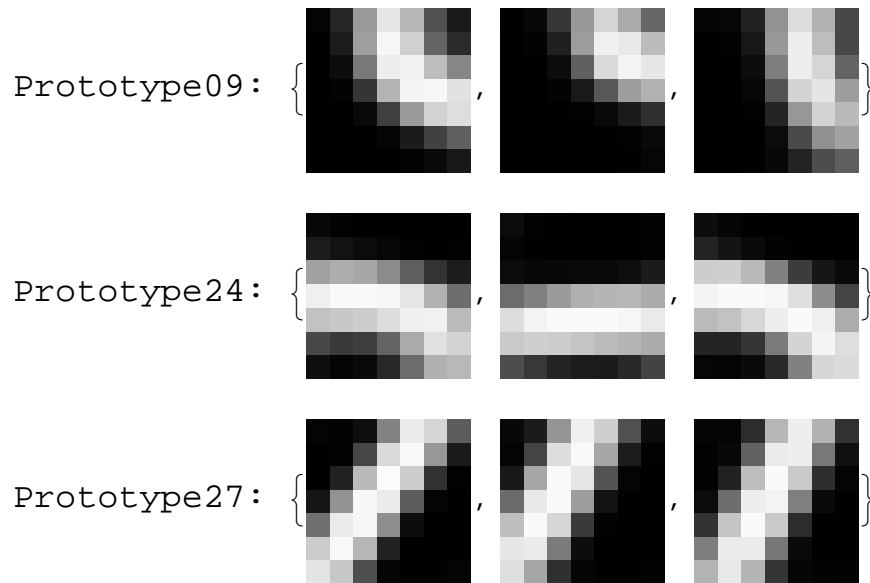


FIGURE 13. Initial computations for three prototypes, (i) Left Column: original prototypes, from Figure 12; (ii) Center Column: modified prototypes, computed within the 32,000 point Data Spheres; (iii) Right Column: principal axes, computed on the 8,000 point Coordinate Spheres.

Figure 12 shows an initial selection of 35 prototypes for the 600,000  $7 \times 7$  patches. The prototypes outlined in blue were selected (subjectively) for a more detailed investigation. (Prototype 02, in which most of the pixels are black, was only used to provide a lower dimensional test case for the development of our algorithms) We will therefore focus our attention on the three examples: Prototype 09, Prototype 24, Prototype 27. The full set of 35 prototypes was constructed by a combination of: (i) `pgrascent` in Figure 7, with `xstart` generated randomly, with  $\beta = 1/8$ , and with a 2000 point `Sample` retrieved by the `NearestFunction` at each iteration; plus (ii) a traditional clustering algorithm (`FindClusters` in *Mathematica*) applied to the output of `pgrascent`; and finally (iii) some manual pruning at the end of the process to eliminate redundancies. We then constructed a 32,000 point Data Sphere around each prototype, and used these for all the subsequent data analyses. Note that  $35 \times 32,000 = 1,120,000$ , so we can potentially partition the entire dataset almost twice over. In fact, an

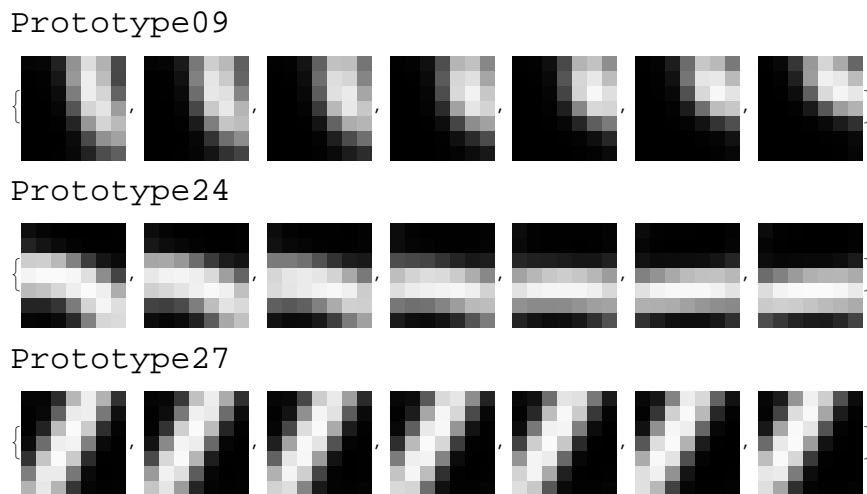


FIGURE 14. The  $\rho$  coordinate curves along the principal axes, for three prototypes.

analysis *ex post* shows that the union of the 32,000 point Data Spheres around these 35 prototypes covers 92.5% of the distinct  $7 \times 7$  patches in our sample. So there is room for some improvement here, but not much.

Although each prototype is located at the center of its Data Sphere, by definition, it will not necessarily be located at a mode of the probability distribution, since we have altered the sample in `pgradascent` to include the nearest 32,000 data points. Thus we now compute the integral curve of  $\nabla U$ , starting at the original prototype, to arrive at a modified prototype, where  $\nabla U(\mathbf{x}) = 0$ . The results are shown in the center column of Figure 13. We then draw a Coordinate Sphere around each modified prototype, and apply Step One of the procedure defined in Section 3 to compute the points at which the  $\rho$  coordinate curves drawn *inwards* to the origin have minimal Riemannian length. These points are shown in the right column of Figure 13. The  $\rho$  coordinate curves themselves are shown in Figure 14.

Table 1 shows the size of the Data Sphere and the Coordinate Sphere for the three *prototypical clusters* that we are analyzing. These values should be compared with the maximal distance in the hypercube ( $\sqrt{49} = 7.0$ ), and with the standard deviation of the kernel density estimator when the smoothing parameter  $\beta = 1$  ( $\sigma = 0.707107$ ).

The distances in Table 2 reveal some of the main properties of our geometric model. The Euclidean distance along each  $\rho$  coordinate

TABLE 1. Radius in the original Euclidean space of the 32,000 point Data Sphere and the 8,000 point Coordinate Sphere, for three prototypical clusters.

	(a) Radius of Data Sphere	(b) Radius of Coordinate Sphere
Prototype 09	2.95906	1.75322
Prototype 24	3.15226	2.30487
Prototype 27	2.97573	1.95364

curve, Column (c) in Table 2, is greater than the Euclidean distance between its two end points, Column (b) in Table 1. This is an indicator of the fact that the principal axis is a curve, and not a straight line. The Riemannian distance inwards along the  $\rho$  coordinate curves, Column (d) in Table 2, is much less than the Euclidean distance in Column (c). This is an indicator of the fact that the principal axis is traversing a region of high probability density. But Column (e) in Table 2, which displays the Riemannian distance computed *outwards* along the  $\rho$  coordinate curve for approximately the same Euclidean distance, is much larger because the probability density in this region is much smaller.

TABLE 2. Distances along the  $\rho$  coordinate curves for the principal axes from a point on the Coordinate Sphere, both inwards and outwards. Compare Figures 13 and 14.

	(c) Euclidean Distance Inwards	(d) Riemannian Distance Inwards	(e) Riemannian Distance Outwards
Prototype 09	2.40866	0.90783	4.01243
Prototype 24	2.90017	0.764126	6.93029
Prototype 27	2.0754	0.38668	3.41653

It is also interesting to analyze Figures 13 and 14 qualitatively. These images were constructed by solving a system of differential equations on pixels in a high-dimensional image space, a very local process, but they seem to possess certain global coherence properties. For Prototype 09, we see a simple geometric shape modified by a shift transformation. The mapping from the left column to the center column in Figure 13 is basically a two-dimensional shift, one pixel up and one pixel to

the right. The mapping from the right column to the center column, which is displayed in Figure 14 as a discretely sampled continuous curve, shifts the same geometric shape up by two pixels. For Prototype 27, we see another simple geometric shape modified by a sequence of global transformations. The mapping from the left column to the center column in Figure 13 is basically a counter clockwise rotation. The lower left corner is fixed, approximately, while the upper end of the geometric shape is shifted one pixel to the left. The mapping from the right column to the center column in Figure 13, which is displayed in Figure 14 as a discretely sampled continuous curve, shifts the same geometric shape one pixel to the left. Prototype 24 is somewhat more complex. Here the discretely sampled continuous mapping in Figure 14 shifts the left half of the geometric shape down by one pixel, while it bends the right half of the geometric shape up to construct a thick horizontal line.

Keeping these coherence properties in mind, let's now look at Step Two and Step Three of the procedure defined in Section 3. In Step Two, we first diagonalize the Riemannian matrix,  $(g_{i,j}(\mathbf{x}))$ , at the points on the principal axes shown in the right column of Figure 13. Taking Prototype 09 as an example, the two eigenvalues are 35.7443 and 13.572, and the infinitesimal eigenvectors are constructed to have unit norm. Thus the integrand of the energy functional for the maximal infinitesimal eigenvector,  $\xi_1$ , is 35.7443. (See Equation (15) in Section 3.) For the minimal infinitesimal eigenvectors, we adopt the following strategy: We generate 10,000 random linear combinations of the eigenvectors,  $\xi_2, \xi_3, \dots, \xi_{48}$ , using Equation (17), we sort these linear combinations by their norms, and we select every 200th entry in the sorted list. We then apply the Gram-Schmidt orthogonalization process (using `Othogonalize` in *Mathematica*) to the selected eigenvectors to construct a set of 47 orthonormal basis vectors. For each of these basis vectors, the integrand of the energy functional is 13.572. (See Equation (18) in Section 3.) Furthermore, since  $\xi_1$  was orthogonal to all of the eigenvectors,  $\xi_2, \xi_3, \dots, \xi_{48}$ , we now have an orthonormal basis for the 48-dimensional tangent subbundle at the point on the principal axis that will serve as the origin of our  $\Theta$  coordinate curves.

Figure 15 displays the  $\Theta$  coordinate curves that were computed in Step Three by solving the Euler-Lagrange equations with the initial directions,  $\mathbf{v}(0)$ , set to the values of the *maximal* infinitesimal eigenvectors,  $\xi_1$ . (The first row for each prototype follows in the positive direction; the second row follows in the negative direction, but this is an arbitrary convention.) The curves are continued until they reach a point at a Euclidean angle of  $\pi/2$  from the origin. Sometimes the

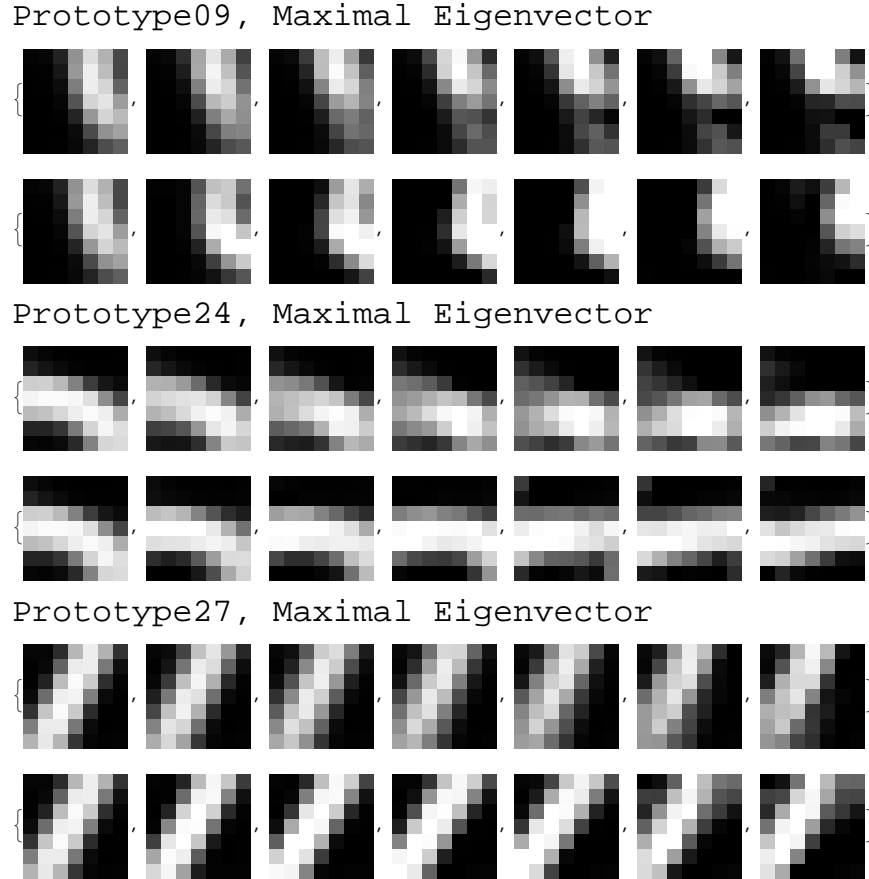


FIGURE 15.  $\Theta$  coordinate curves for the maximal infinitesimal eigenvectors. The first row in each case shows the coordinate curve in the direction of the infinitesimal eigenvector, to the Euclidean angle  $\pi/2$ ; the second row shows the coordinate curve in the opposite direction, to the Euclidean angle  $-\pi/2$ .

computation encounters a singularity in the value of  $P_0(\mathbf{x})$ , and it is necessary to shift the “center” of the coordinate system to a different coordinate axis in order to continue with the algorithm, but this does not happen more than once for each of these curves. Table 3 shows the distances along the coordinate curves to the Euclidean angles  $\pi/2$  in the positive direction and  $-\pi/2$  in the negative direction. Recall that the Riemannian and Euclidean distances computed along a geodesic curve on the Frobenius integral manifold are the same, since each

point on the manifold is a constant Riemannian distance from the origin. Thus there is only a single entry for the distances in Table 3, for each direction.

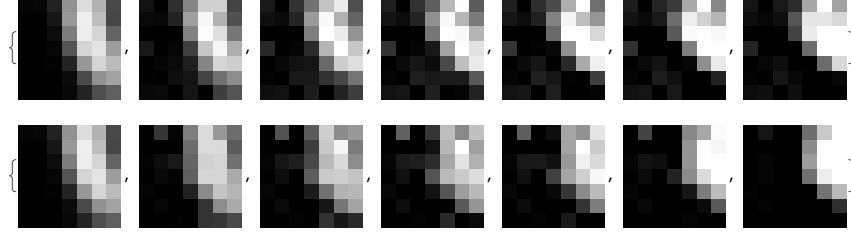
TABLE 3. Riemannian and Euclidean distances along the  $\Theta$  coordinate curves for the maximal infinitesimal eigenvectors, from the principal axis to the Euclidean angles  $\pi/2$  and  $-\pi/2$ . Compare Figure 15.

	Positive Direction	Negative Direction
Prototype 09	2.22261	4.16981
Prototype 24	2.71304	3.58147
Prototype 27	2.10106	2.46165

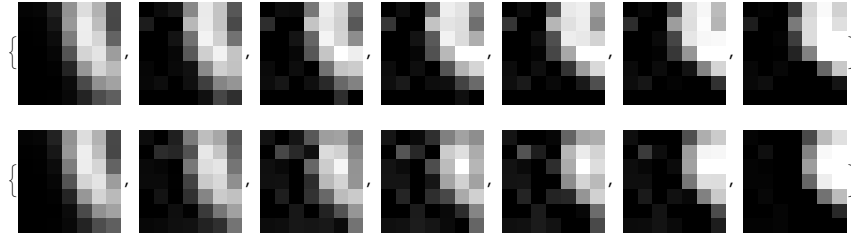
For the *minimal* infinitesimal eigenvectors, we will work exclusively with Prototype 09, as an example, but we will compute all 47  $\Theta$  coordinate curves. (Note: All calculations up to this point have used a 1600 point sample, following a comparison of the results for two 800 point samples. However, when we double the size of the sample from 800 to 1600, we increase the size of the data structures in Figure 10 by a factor of four, and we also increase the CPU time to find a solution to the Euler-Lagrange equations, empirically, by a factor of four. Thus, since we are now computing 47 geodesics, in two directions, we will reduce the computational burden by restricting our analysis here to a single 800 point sample.) Figure 16 shows the three  $\Theta$  coordinate curves with the smallest Riemannian and Euclidean distances in the positive direction, which also happen to be the curves that have the largest Riemannian and Euclidean distances in the negative direction. Table 4 shows these distances, up to the Euclidean angles  $\pi/2$  and  $-\pi/2$ , respectively. The total distance is shown in the third column. Note that the total distance along the  $\Theta$  coordinate curve for the maximal infinitesimal eigenvector in Prototype 09, according to Table 3, is considerably larger: 6.39242.

Figure 17 shows another way to understand the relationship between the curves in Figures 14, 15 and 16: a three-dimensional visualization. How to map 49 dimensions down to three? The black dot at the origin is the modified Prototype 09 in the center column of Figure 13. The 49-dimensional image space is rotated around the origin to align the  $x$  axis with the principal axis, so that the coordinates at the tip of the red arrow are  $(1.75322, 0, 0)$ , where 1.75322 is the radius of the Coordinate Sphere, as shown in Table 1. For the  $y$  coordinate, we rotate the image

Prototype09, Curve 16



Prototype09, Curve 17



Prototype09, Curve 9

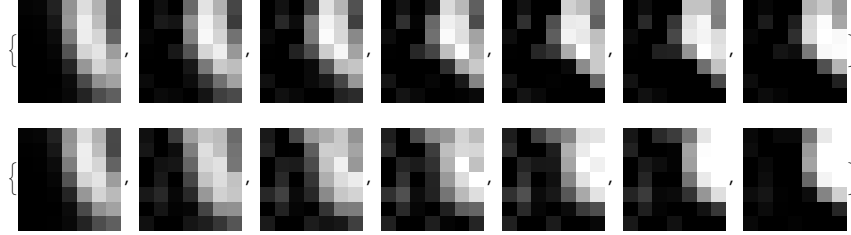


FIGURE 16. The three minimal positive  $\Theta$  coordinate curves for Prototype 09. The first row in each case shows the coordinate curve in the direction of the positive infinitesimal eigenvector, to  $\pi/2$ ; the second row shows the coordinate curve in the opposite direction, to  $-\pi/2$ .

TABLE 4. Prototype 09: Riemannian and Euclidean distances along the  $\Theta$  coordinate curves to  $\pi/2$  and  $-\pi/2$  for three minimal infinitesimal eigenvectors. Compare Figure 16.

	Positive Direction	Negative Direction	Total Distance
Curve 16	2.61453	3.16092	5.77545
Curve 17	2.68326	3.17738	5.86064
Curve 09	2.68949	3.11284	5.80233

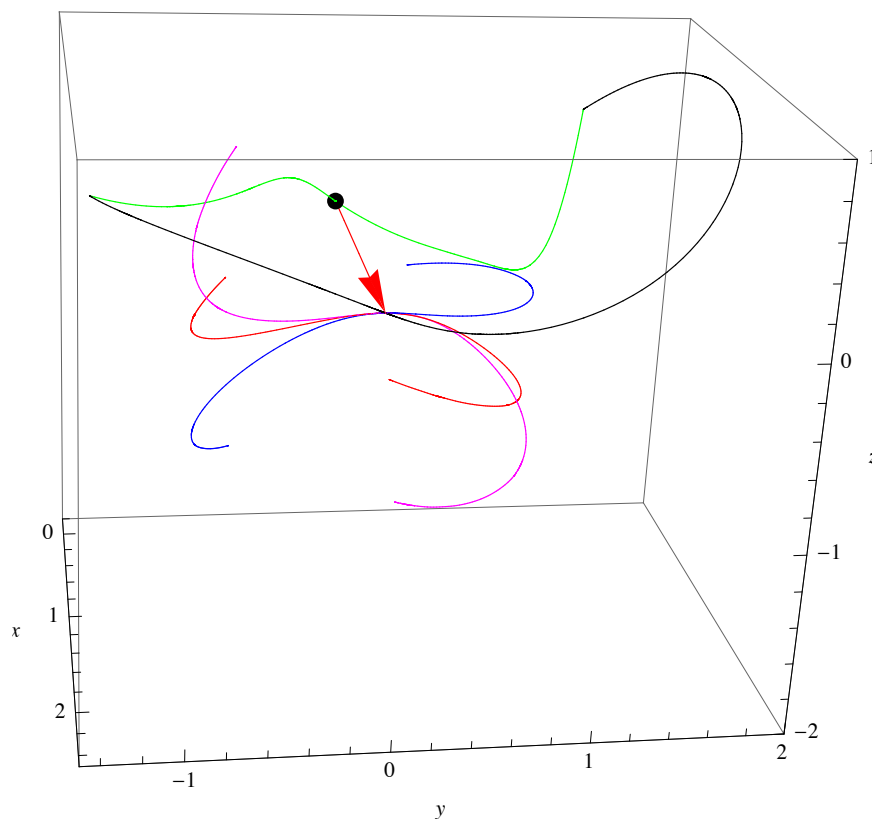


FIGURE 17. A three-dimensional visualization of the coordinate curves for Prototype 09. The curves in Figure 16 are coded by color: *Red* is Curve 16, *Magenta* is Curve 17, *Blue* is Curve 9. The *Black* curve is the  $\Theta$  coordinate curve for the maximal infinitesimal eigenvector, as shown in Figure 15, and the *Green* curves are the  $\rho$  coordinate curves at the Euclidean angles  $\pi/2$  and  $-\pi/2$  from the origin.

space again around the tip of the red arrow to align the  $y$  axis with the infinitesimal eigenvectors that are used to generate the  $\Theta$  coordinate curves, but we do this separately for each curve. Thus, although the initial directions of the four curves depicted in Figure 17 are mutually orthogonal in the 49-dimensional image space, in the visualization they are all drawn in the same plane. Finally, we need to collapse the remaining 47 dimensions down to the  $z$  axis, somehow. Our solution is simply to sum all the remaining coordinates after applying the  $x$  and  $y$  rotations to the first two, which means that the initial value

of  $z$  at the tip of the red arrow will be zero, and the length of the curves in the image space will correspond roughly to the length of the curves in the visualization. In the image space, the coordinate curves are extended to the Euclidean angles  $\pi/2$  and  $-\pi/2$ , and this is true in the visualization as well. Note that the positive direction towards  $\pi/2$  corresponds to a clockwise rotation in the visualization, as can be seen by comparing the length of the two segments of the black curve in Figure 17.

The green curves in Figure 17 also illustrate some of the main properties of our geometric model. These are the  $\rho$  coordinate curves drawn inwards from the points on the  $\Theta$  coordinate curve for the maximal infinitesimal eigenvector at the Euclidean angles  $\pi/2$  and  $-\pi/2$ . The Euclidean distance along the curve from  $\pi/2$  (on the left) is 1.50939 and the Riemannian distance is 0.947386. The Euclidean distance along the curve from  $-\pi/2$  (on the right) is 2.1958 and the Riemannian distance is 0.922917. These values should be compared to the values in Table 2 for the corresponding distances along the principal axis for Prototype 09: The Euclidean distances in Figure 17 are less, but the Riemannian distances are approximately the same (within the tolerance of our numerical calculations). This is a reflection of the fact that the geodesics on the Frobenius integral manifold are a constant Riemannian distance from the origin.

We saw in our analysis of the three-dimensional curvilinear Gaussian example in Section 3 that the “optimal”  $\Theta$  coordinate curve was the one with the minimal Riemannian or Euclidean length, when measured at a fixed Euclidean angle from the origin. What choices does this principle suggest for Prototype 09? Looking at Table 3 for the maximal infinitesimal eigenvector, we see that the distance in the positive direction for Prototype 09 is less than all of the distances in Table 4, but the distance in the negative direction is greater than all of the distances in Table 4. Thus the principle seems to be inconclusive in this case. In constructing Table 4 for the minimal infinitesimal eigenvectors, however, we chose the three curves with the smallest distances in the positive direction and the largest distances in the negative direction, and it is instructive to look at these choices as they are displayed in Figure 16. Qualitatively, all three curves, 16, 17, and 9, seem to be more compact and coherent in the positive direction than in the negative direction, which is consistent with the principle developed in Section 3. But in this case, we have additional choices. Table 5 lists the ten  $\Theta$  coordinate curves for which the total distance is minimal. Although we do not have the space to display these examples, they

are in both directions qualitatively similar to the curves in the positive direction in Figure 16.

TABLE 5. Prototype 09: The ten  $\Theta$  coordinate curves with the least total Riemannian and Euclidean distances from the principal axis to  $\pi/2$  and  $-\pi/2$ .

	Positive Direction	Negative Direction	Total Distance
Curve 42	2.80639	2.77794	5.58433
Curve 23	2.77045	2.81585	5.58631
Curve 30	2.79071	2.79673	5.58744
Curve 37	2.77144	2.81653	5.58799
Curve 29	2.8927	2.69908	5.59179
Curve 44	2.83735	2.75788	5.59523
Curve 11	2.70893	2.88847	5.59741
Curve 36	2.80777	2.79319	5.60096
Curve 26	2.71708	2.88505	5.60213
Curve 01	2.69536	2.90715	5.60251

Thus, for an “optimal” 12-dimensional coordinate system for Prototype 09, a reasonable choice would be: (i) the  $\rho$  coordinate; (ii) the  $\Theta$  coordinate in Table 3, which is depicted in Figure 15; and (iii) the ten  $\Theta$  coordinates in Table 5.

It may also be instructive to compare Figures 14, 15 and 16 to the results that would be obtained from Principal Component Analysis [Pea01]. Figure 18 shows the first six principal eigenvectors computed on the covariance matrix for the 32,000 point Data Sphere around Prototype 09. The first two eigenvectors show some similarities to the curves for Prototype 09 in Figures 14 and 15. But the subsequent eigenvectors are very different, and they do not seem to be related to any coherent global geometric shapes in the MNIST Dataset.

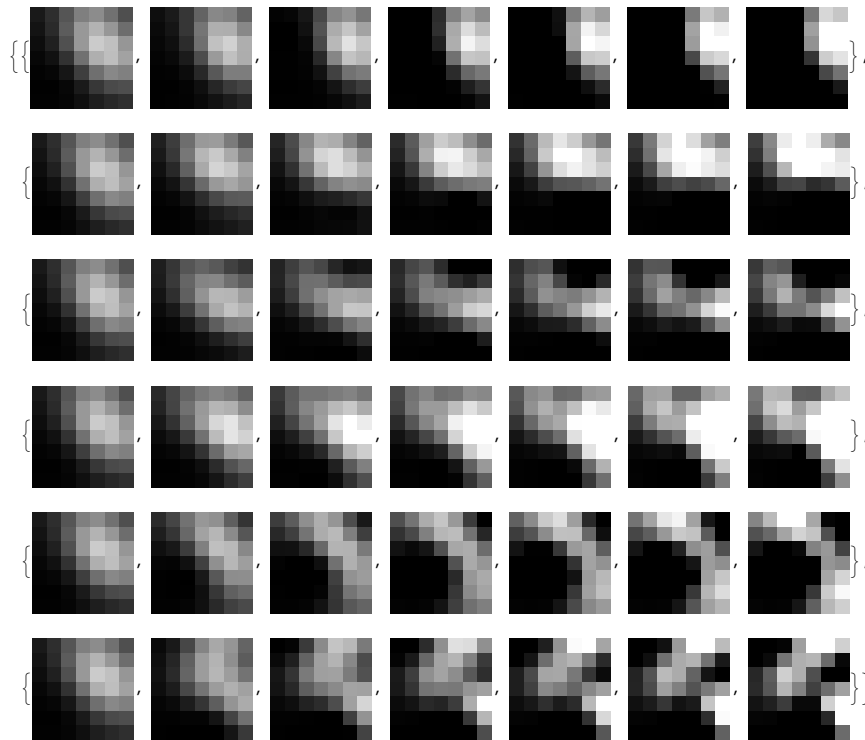


FIGURE 18. Principal eigenvectors for the covariance matrix computed on the 32,000 point Data Sphere for Prototype 09.

#### REFERENCES

- [AB14] G. Alain and Y. Bengio. What regularized auto-encoders learn from the data generating distribution. *Journal of Machine Learning Research*, 15:3743–3773, 2014.
- [AM77] L. Auslander and R. E. MacKenzie. *Introduction to Differentiable Manifolds*. Dover Publications, 1977.
- [BC01] R. L. Bishop and R. J. Crittenden. *Geometry of Manifolds*. American Mathematical Society, 2nd edition, 2001.
- [BCV13] Y. Bengio, A. Courville, and P. Vincent. Representation learning: A review and new perspectives. *IEEE Transactions on Pattern Analysis and Machine Intelligence*, 35(8):1798–1828, 2013.
- [BG68] R. L. Bishop and S. I. Goldberg. *Tensor Analysis on Manifolds*. Macmillan, 1968.
- [BN03] M. Belkin and P. Niyogi. Laplacian eigenmaps for dimensionality reduction and data representation. *Neural Computation*, 15(6):1373–1396, 2003.
- [BN05] M. Belkin and P. Nyogi. Towards a theoretical foundation for Laplacian-based manifold methods. In *Proceedings of the Conference on Learning Theory (COLT)*, pages 486–500, 2005.

- [Bra03] M. Brand. Charting a manifold. In *Advances in Neural Information Processing Systems*, volume 15, pages 961–968, 2003.
- [Che95] Y. Cheng. Mean shift, mode seeking, and clustering. *IEEE Transactions on Pattern Analysis and Machine Intelligence*, 17(8):790–799, 1995.
- [CL06] R. R. Coifman and S. Lafon. Diffusion maps. *Applied and Computational Harmonic Analysis*, 21:5–30, 2006.
- [CM02] D. Comaniciu and P. Meer. Mean shift: A robust approach toward feature space analysis. *IEEE Transactions on Pattern Analysis and Machine Intelligence*, 24(5):603–619, 2002.
- [Coa12] A. Coates. *Demystifying Unsupervised Feature Learning*. PhD thesis, Stanford University, 2012.
- [CSP<sup>+</sup>10] M. Chen, J. Silva, J. W. Paisley, C. Wang, D. B. Dunson, and L. Carin. Compressive sensing on manifolds using a nonparametric mixture of factor analyzers: Algorithm and performance bounds. *IEEE Transactions on Signal Processing*, 58(12):6140–6155, 2010.
- [CZF10] C. Chen, J. Zhang, and R. Fleischer. Distance approximating dimension reduction of Riemannian manifolds. *IEEE Transactions on Systems, Man, and Cybernetics (Part B)*, 40(1):208–217, 2010.
- [DG03] D. Donoho and C. Grimes. Hessian eigenmaps: Locally linear embedding techniques for high-dimensional data. *Proceedings of National Academy of Sciences*, 100:5591–5596, 2003.
- [Fey48] R. P. Feynman. Space-time approach to non-relativistic quantum mechanics. *Reviews of Modern Physics*, 20:367–387, 1948.
- [FH65] R. P. Feynman and A.R. Hibbs. *Quantum Mechanics and Path Integrals*. McGraw-Hill, 1965.
- [FH75] K. Fukunaga and L. D. Hostetler. The estimation of the gradient of a density function, with applications in pattern recognition. *IEEE Transactions on Information Theory*, 21(1):32–40, 1975.
- [FMN16] C. Fefferman, S. Mitter, and H. Narayanan. Testing the manifold hypothesis. *Journal of the American Mathematical Society*, 29(4):983–1049, 2016.
- [HA<sub>v</sub>L07] M. Hein, J.-Y. Audibert, and U. von Luxburg. Graph Laplacians and their convergence on random neighborhood graphs. *Journal of Machine Learning Research*, 8:1325–1368, 2007.
- [HR03] G. E. Hinton and S. T. Roweis. Stochastic neighbor embedding. In *Advances in Neural Information Processing Systems*, volume 15, pages 833–840, 2003.
- [Ito51] K. Ito. *On Stochastic Differential Equations*. Number 4 in Memoirs of the American Mathematical Society. A.M.S., Providence, R.I., 1951.
- [Kac49] M. Kac. On distributions of certain Wiener functionals. *Transactions of the American Mathematical Society*, 65:1–13, 1949.
- [Kol31] A.N. Kolmogorov. Über die analytischen Methoden in der Wahrscheinlichkeitsrechnung. *Mathematische Annalen*, 104:415–458, 1931.
- [Kri09] A. Krizhevsky. Learning multiple layers of features from tiny images. Technical report, Department of Computer Science, University of Toronto, 2009.
- [Lan95] S. Lang. *Differential and Riemannian Manifolds*. Graduate Texts in Mathematics, 160. Springer-Verlag, 1995.

- [LBBH98] Y. LeCun, L. Bottou, Y. Bengio, and P. Haffner. Gradient-based learning applied to document recognition. *Proceedings of the IEEE*, 86(11):2278–2324, 1998.
- [LW10] A. B. Lee and L. Wasserman. Spectral connectivity analysis. *Journal of the American Statistical Association*, 105(491):1241–1255, 2010.
- [McC14] L. T. McCarty. Clustering, coding, and the concept of similarity. *Preprint*, arXiv:1401.2411v1 [cs.LG], 2014.
- [McC18] L. T. McCarty. Clustering, coding, and the concept of similarity (Version 2.0). *Preprint*, arXiv:1401.2411v2 [cs.LG], 2018.
- [OF96] B. A. Olshausen and D. J. Field. Emergence of simple cell receptive field properties by learning a sparse code for natural images. *Nature*, 381:607–609, 1996.
- [Pea01] K. Pearson. On lines and planes of closest fit to systems of points in space. *Philosophical Magazine*, 2:559–572, 1901.
- [Ran09] M. A. Ranzato. *Unsupervised Learning of Feature Hierarchies*. PhD thesis, New York University, 2009.
- [RDV<sup>+</sup>12] S. Rifai, Y. Dauphin, P. Vincent, Y. Bengio, and X. Muller. The manifold tangent classifier. In *Advances in Neural Information Processing Systems*, volume 24, pages 2294–2302, 2012.
- [RS00] S. T. Roweis and L. K. Saul. Nonlinear dimensionality reduction by locally linear embedding. *Science*, 290(5500):2323–2326, 2000.
- [Spi99] M. Spivak. *A Comprehensive Introduction to Differential Geometry*, volume 1. Publish or Perish, Inc., 3rd edition, 1999.
- [SSM98] B. Schölkopf, A. Smola, and K.-R. Müller. Nonlinear component analysis as a kernel eigenvalue problem. *Neural Computation*, 10(5):1299–1319, 1998.
- [ST94] D. W. Stroock and S. Taniguchi. Diffusions as integral curves, or Stratonovich without Itô. In *The Dynkin Festschrift. Markov processes and their applications. In celebration of Eugene B. Dynkin's 70th birthday*, pages 333–369. Boston, MA: Birkhäuser, 1994.
- [ST96] D. W. Stroock and S. Taniguchi. Diffusions as integral curves on manifolds and Lie groups. In *Probability theory and mathematical statistics. Lectures presented at the semester held in St. Petersburg, Russia, March 2–April 23, 1993*, pages 219–226. Amsterdam: Gordon and Breach Publishers, 1996.
- [Str66] R. L. Stratonovich. A new representation for stochastic integrals and equations. *SIAM Journal on Control*, 4(2):362–371, 1966.
- [Str93] D. W. Stroock. *Probability Theory: An Analytic View*. Cambridge University Press, 1993.
- [TB99] M. E. Tipping and C. M. Bishop. Mixtures of probabilistic principal component analyzers. *Neural Computation*, 11(2):443–482, 1999.
- [THJ10] D. Ting, L. Huang, and M. I. Jordan. An analysis of the convergence of graph Laplacians. In *Proceedings of the 27th International Conference on Machine Learning (ICML)*, pages 1079–1086, 2010.
- [TJ18] D. Ting and M. I. Jordan. On nonlinear dimensionality reduction, linear smoothing and autoencoding. *Preprint*, arXiv:1803.02432v1 [stat.ML], 2018.

- [TSL00] J. B. Tenenbaum, V. Silva, and J. C. Langford. A global geometric framework for nonlinear dimensionality reduction. *Science*, 290(5500):2319–2323, 2000.
- [Vin14] P. Vincent. A connection between score matching and denoising autoencoders. *Neural Computation*, 23(7):1661–1674, 2014.
- [WS06] K. Q. Weinberger and L. K. Saul. Unsupervised learning of image manifolds by semidefinite programming. *International Journal of Computer Vision*, 70(1):77–90, 2006.
- [YZG10] K. Yu, T. Zhang, and Y. Gong. Nonlinear learning using local coordinate coding. In *Advances in Neural Information Processing Systems*, volume 22, pages 2223–2231, 2010.
- [ZZ04] Z. Zhang and H. Zha. Principal manifolds and nonlinear dimension reduction via local tangent space alignment. *SIAM Journal on Scientific Computing*, 26(1):313–338, 2004.